Physics – Uspekhi **39** (4) 393 – 416 (1996)

CONFERENCES AND SYMPOSIA PACS numbers: 01.10.Fv

Scientific Session of the Division of General Physics and Astronomy of the Russian Academy of Sciences (29 November 1995)

A scientific session of the Division of General Physics and Astronomy of the Russian Academy of Sciences was held on 29 November 1995 at the P L Kapitza Institute of Physical Problems. Six papers were presented at this session:

(1) **N N Ledentsov, V M Ustinov, S V Ivanov, B Ya Mel'tser, M V Maksimov, P S Kop'ev, Zh I Alferov** (A F Ioffe Institute of Physics and Technology, Russian Academy of Sciences, St.-Petersburg), **D Bimberg** (Institut für Festkörperphysik, Technische Universität Berlin, Berlin, Germany) "Ordered quantum-dot arrays in semiconducting matrices";

(2) **V T Dolgopolov** (Institute of Solid State Physics, Russian Academy of Sciences, Chernogolovka, Moscow Region) "Percolation metal-dielectric transitions in two-dimensional electron systems";

(3) **V S Dneprovskiĭ** (Department of Physics, Moscow State University, Moscow) "Nonlinear optical properties of semiconducting quantum wires and dots";

(4) **S N Artemenko, A F Volkov, S V Zaitsev-Zotov** (Institute of Radio Engineering and Electronics, Russian Academy of Sciences, Moscow) "Quasi-one-dimensional conductors with a charge density wave";

(5) **V V Dobrovitskiĭ** (Department of Physics, Moscow State University, Moscow), **A K Zvezdin** (Institute of General Physics, Russian Academy of Sciences, Moscow), **A F Popkov** (State Institute of Physical Problems, Zelenograd, Moscow Region) "Giant magnetoresistance, spin-reorientation transitions, and macroscopic quantum phenomena in magnetic nanostructures";

(6) **V I Belyavskiĭ, Yu V Kopaev, N V Kornyakov** (P N Lebedev Physical Institute, Russian Academy of Sciences, Moscow) "Controlled modulation of the binding energy of impurity states in a quantum-well system".

An abridged version of the papers is given below.

PACS numbers: 73.20.Dx, **73.90.+f**

Ordered quantum-dot arrays in semiconducting matrices

N N Ledentsov, V M Ustinov, S V Ivanov,
B Ya Mel'tser, M V Maksimov, P S Kop'ev,
D Bimberg, Zh I Alferov

1. Introduction

The use of semiconducting materials revolutionised micro- and optoelectronics. The high density of atoms in the crystal enables achievement of high electron and hole concentrations by doping the semiconductor, allows intensive electric currents with low dissipation of energy, and leads to high fundamental-absorption coefficients and, hence, elevated amplification levels on population inversion. These properties are important, for example, in photodetector or injection laser applications. The invention [1 – 3] and realisation [4 – 6] of 'ideal' defect-free heterostructures have extended qualitatively the range of possibilities in the control of electron currents and light fluxes in a crystal.

The high density of atoms has certain obvious consequences, however, which are often adverse to device functioning. In a crystal, the discrete atomic levels peculiar to gas phase are split into wide bands giving rise to allowed transitions, the ultimate reason being that the high atomic density causes an interaction between the electron shells. This tends to charge-carrier 'energy spread' with increasing temperature and accordingly degrades the characteristics of most micro- and optoelectronic devices. In a heterolaser, for example, such energy spread reduces the gain at a fixed concentration of injected carriers and thus necessitates a higher injection current density for maintaining the generation regime.

A certain improvement in the characteristics of semiconducting devices has been achieved by providing the active region of a device with ultrathin layers exhibiting dimensional quantisation effects. In this case the initially continuous charge-carrier energy spectrum splits into a number of discrete subbands in the direction of the dimensional quantisation axis. For a single infinite-wall quantum well, the energy spectrum takes the form

$$E = \frac{\hbar^2}{2m^*}\left(\frac{\pi n}{L_z}\right)^2 + \frac{(\hbar k_{x,y})^2}{2m^*}\,, \quad n = 1, 2, 3, \ldots, \tag{1}$$

where m^* is the effective mass of the carrier, L_z is the thickness of the dimensionally-quantized layer, and $k_{x,y}$ is the charge-carrier wave vector parallel to the layer plane. The first term characterises the discrete electronic spectrum in the direction of the quantisation axis, the second one describes the continuous energy spectrum of the infinite motion the carrier performs in the layer plane.

Dimensional quantisation modifies markedly the electronic spectrum in a crystal. The density of states near the bottom of a dimensionally-quantized subband, rather than being parabolically increased with energy, now goes in steps. If the energy difference between two different subbands of dimensional quantisation exceeds the thermal energy (kT), the deterioration of device characteristics with temperature is somewhat less than in the bulk material. For example, in the best-quality quantum-dimensional lasers the characteristic temperature T_0, which describes the exponential growth of the threshold current with increasing temperature, is about two to three times that of a thick-layer laser and may be as

Uspekhi Fizicheskikh Nauk **166** (4) 423–448 (1996)
Translated by E G Strel'chenko, edited by A Radzig

high as 240 K. The use of quantum wells has also improved the mode stability and dynamical characteristics, and reduced the threshold current density down to ~ 50 A cm^{-2} at 300 K [7]. Still, the problem of the carrier scattering in a wide energy 'window' is not yet cardinally resolved.

2. General requirements on quantum-dot structures

The future of semiconducting devices is associated with the use of structures of less than two dimensions, i.e. quantum wires and, in particular, quantum dots. The quantum dot makes up a crystallite which can also be thought of as a large 'semiconducting atom' containing from thousands to hundreds of thousands of ordinary atoms. The energy spectrum of a charge carrier for such a system must be described by a set of completely discrete energy levels

$$E = \delta(n), \quad \text{where} \quad n = 0, 1, 2, 3, \ldots \tag{2}$$

Accordingly, the absorption and emission spectra of the quantum dot would constitute a collection of narrow lines whose width is determined by the carrier lifetime in the dot, for example, by the exciton radiative annihilation time. Thermal broadening is completely absent here.

Both the observation of quantum-mechanical effects and the realisation of corresponding device structures depend on whether 'ideal' quantum dots can be prepared. For most applications quantum dots must be placed in a semiconducting matrix, this latter allowing carriers to be current-injected into a dot (the glass-matrix semiconducting quantum dots of the pioneering studies [8] are of limited practical use and the glass-semiconductor interface cannot in principle be considered as defect-free). It is desirable that the dimensional quantisation levels of the carriers be separated by more than 2–3 kT at room temperature, in order to prevent temperature-activated population of the higher levels. For most semiconducting compounds this places the effective dot 'radius' within 50 A. On the other hand, the lowest carrier level in the dot must incorporate as large localisation energy as possible with respect to the continuum (i.e., to the edge of the corresponding matrix-material band). Otherwise, an increase in temperature will cause a thermally activated escape of carriers from the dots. Moreover, the dots must possess defectless heteroboundaries and be free of nonradiative recombination centres — requirements which cannot in general be achieved unless by direct methods of fabrication. To provide high maximum gain magnitudes requires production of *dense* arrays of *heterogeneous* quantum dots in the substrate plane (for injection heterolasers) and/or perpendicular to it (which is of particular importance for surface and cascade lasing behaviour and for all types of photodetectors).

3. Quantum-dot structure preparation

3.1. Methods

Various quantum-dot preparation techniques, such as selective etching of quantum-well structures or shaped-surface growth, have been employed. It turned out, however, that the most promising methods are direct ones using spontaneous nanostructure formation effects such as growth on microscopically-ordered faceted surfaces [9], formation of ordered monolayer-domain structures under submonolayer depositions [10], and in particular formation of ordered quantum-wire (dot) arrays via spontaneous morphological transformation of an elastic-stressed layer [11]. In the last case, three-dimensional islands coherent with the substrate, form (Fig. 1).

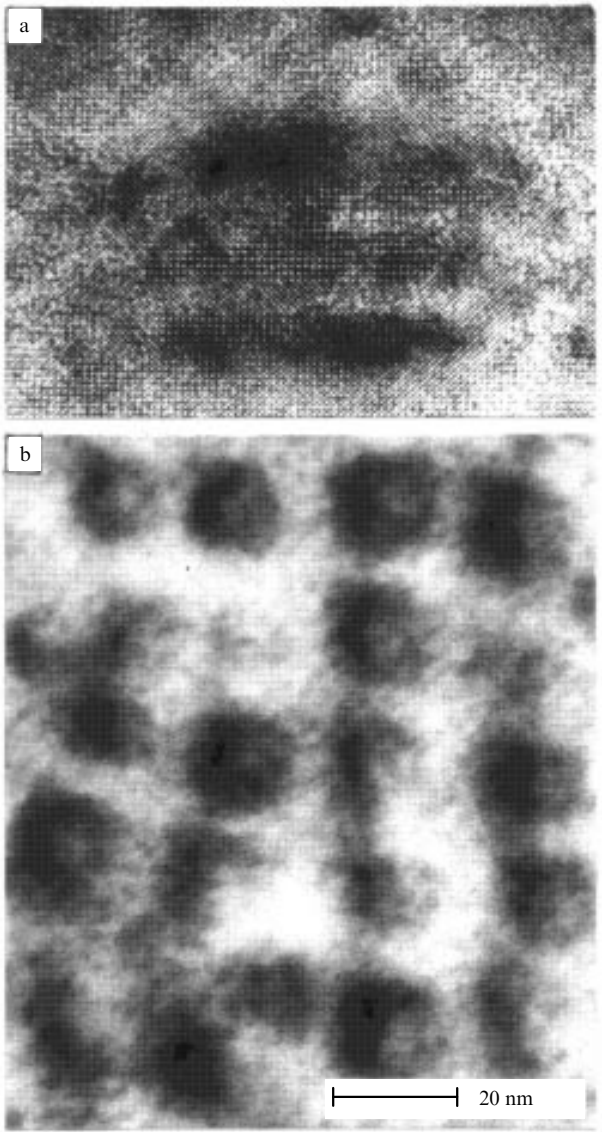

Figure 1. (a) Image in the cross section along [010] axis for an array of quantum dots tunnel-coupled in the z-direction ([100]), which was obtained by high-resolution transmission electron spectroscopy (TES). Dots were produced on three-stage deposition of InAs layers 5 A thick in average, which were separated by GaAs deposited layers 15 A in average thickness; (b) TES micrograph of the same structure (top view). InAs dots are arranged in the substrate plane into a primitive lattice with principal axes along the [010] and [100] directions.

Surprisingly, the islands produced at the substrate surface (which, in the case of the Stransky–Krastanov growth mechanism, is 'wetted' by a thin layer of elastic-stressed material) have been found to be highly uniform in shape and size as well as being ordered in terms of their relative positions [11, 12]. This fact undoubtedly opens up fundamentally new possibilities both in basic and applied studies of zero-dimensional structures.

3.2. The nature of forming the ordered quantum-dot structures

Spontaneous formation of surface nanostructures has long attracted the attention of physicists. The spontaneous formation of ordered arrays of facets at crystal surfaces was first predicted in the works of Andreev and Marchenko [13, 14],

who showed that if the faceting of a surface is energetically favourable, then, taking into account the edge-end relaxation of the intrinsic stresses of the surface, the faceting must always be periodic. Later on Marchenko [15] also showed that for a plane surface carrying two coexistent phases with different magnitudes of the surface friction tensor, the elastic domain-boundary relaxation of surface stresses energetically favours the occurrence of periodic ('parquet') surface structures. In both the faceting and parqueting situations, the total surface area of the island (facet) system does not change as the characteristic period is varied. In this sense, the formation of *three-dimensional islands* differs *qualitatively* from the first two cases. Its driving force is the elastic relaxation in the volume of the stressed island, which is possible if a *three-dimensional* island forms. For a fixed amount of deposited material, the elastic relaxation of the stresses arising from the mismatch of the island and substrate lattice parameters is a function of the *shape* rather than the size of the island. At the same time, the total surface area of the *system of islands increases* as the characteristic island size *is decreased*. The energetically favourable process in this case is the continuous (in time) growth of the characteristic island size due to the evaporation of the smaller islands. Until recently, this approach has appeared to be quite justified, and the experimentally founded small island size dispersion has been linked to kinetic restrictions.

On the other hand, the surface energy of an elastic-stressed layer may differ significantly from that of the relaxed material, the difference being expressible in simplified form as

$$E = -\tau\varepsilon + S\varepsilon^2, \tag{3}$$

where ε is the strain, τ is the surface friction coefficient, which may be either positive (the surface is initially 'extended' at $\varepsilon = 0$) or negative (the surface is 'compressed'), and S is a numerical factor. Estimates show that, for typical values of τ and S in crystals and for strains on the order of or more than 10%, the second term, which is generally positive, becomes dominant [16]. As first shown by Shchukin et al. [12], the dramatic increase of the surface energy in the elastic-stressed layer plays a leading part in the formation of arrays of shape- and size-*ordered* islands. An *increase in the* total *area* of the surface of the system is accompanied in this case by the elastic *relaxation* of the island material deformation ε and, as a consequence, by a *decrease in the surface energy per unit area* of the lateral surfaces of the islands as opposed to the surface of the elastic-stressed wetting layer. Thus, for quite realistic parameters, the total energy of the system of islands may *decrease* as the *total surface area* of this system *increases* due to the reduction in the characteristic size of individual islands (until the short-range potentials formed by the edge ends of the islands–crystallites begin to contribute). At small island sizes, the edge-end relaxation of surface stresses may be another size-ordering factor [12, 13]. In view of the *repulsive interactions between the islands via the elastic-anisotropic substrate*, to the energy minimum there corresponds, in this case, a laterally ordered array of three-dimensional islands all identical in size and shape [12]. At the (001) surface of a cubic crystal, the energetically favourable process is the ordering of the islands into a primitive two-dimensional lattice with principal axes along the *least-stiffness* directions [100] and [010]. The elastic anisotropy of the substrate is also responsible for the shape of an individual island, which has a square base with sides along [100] and [010] axes. The lateral sides are determined by {011} or {023} facets. The preservation of a compact shape is energetically favourable, since it enables a large energy gain at the expense of elastic stress relaxation (for {011} facets, the relaxation is 60% of the total elastic energy of the stressed layer [12]) without too large an increase in surface area.

Figure 1a presents a high-resolution transmission electron spectroscopy (TES) image of the cross section (along the [010] direction) of an array of quantum dots tunnel-coupled in the z-direction ([100]), whose substrate plane arrangement is that of a primitive two-dimensional lattice (Fig. 1b, TES micrograph, top view) with [010] and [100] principal axes [13]. The formation of tunnel-coupled islands (for example, InAs islands in a GaAs matrix) proceeds as follows: a partial overgrowing (closure) of an island (to about 1/4 – 1/2 of its full height) increases elastic stresses in the volume of the island and introduces into the picture the thermodynamic tendency of the stressed material to 'surface' from the overgrown to the non-overgrown part, with a corresponding replacement of the former by the atoms of an intermediate GaAs layer. Repeated InAs and GaAs depositions lead to a multiple splitting of the stressed island thus forming a structure of a number of tunnel-coupled parts as shown in Fig. 1a [17]. At the same amount of InAs per deposition cycle, the upper islands are of somewhat larger size due to InAs being in part mass-transferred from the lower parts.

4. Optical properties of structures with three-dimensional ordered quantum-dot arrays

4.1. Luminescence of three-dimensional quantum-dot arrays

Figure 2a shows the photoluminescence (PL) spectra of lamellar structures which are grown with one (QD1), two (QD2), three (QD3), and four (QD4) InAs deposition cycles and which have an average layer thickness of 1.7 ML and are divided by GaAs interlayers of 25 A average thickness. For an intermediate GaAs layer of such a thickness, the splitting of a pyramidal island leads to the formation of a set of islands closely-spaced in the vertical direction. The electron and hole states of neighbouring islands are coupled, and this, owing to the resulting decrease in the dimensional quantisation energy for the electron and hole ground states, exactly produces a long-wave shift of the quantum-dot PL line in the case of several InAs layers being deposited. A similar effect is observed for the corresponding peak in the calorimetric absorption spectrum [17]. Simultaneously, there is a sharp decrease in the exciton radiative recombination lifetime in a quantum dot [17].

Increasing the width of the GaAs layer leads to a short-wave shift of the PL line (Fig. 2b). This is due to the reduced interaction between carriers localised on neighbouring dots. As the width of the GaAs layer varies from ~ 10 A to ~ 25 A, the line shift is not very significant, but rising to ~ 45 A causes a marked (~ 40 MeV) shift to higher energies. Notice that the line peak does not reach a position characteristic of a single InAs deposition cycle, implying that tunnelling effects are important in this case as well.

4.2. Injection heterolasers based on three-dimensional tunnel-coupled dot arrays

As an illustration of a possible use of three-dimensional arrays of tunnel-coupled quantum dots, let us consider the operating characteristics of injection heterolasers. Lasers with single-plane active region and (In, Ga)As/GaAs quantum

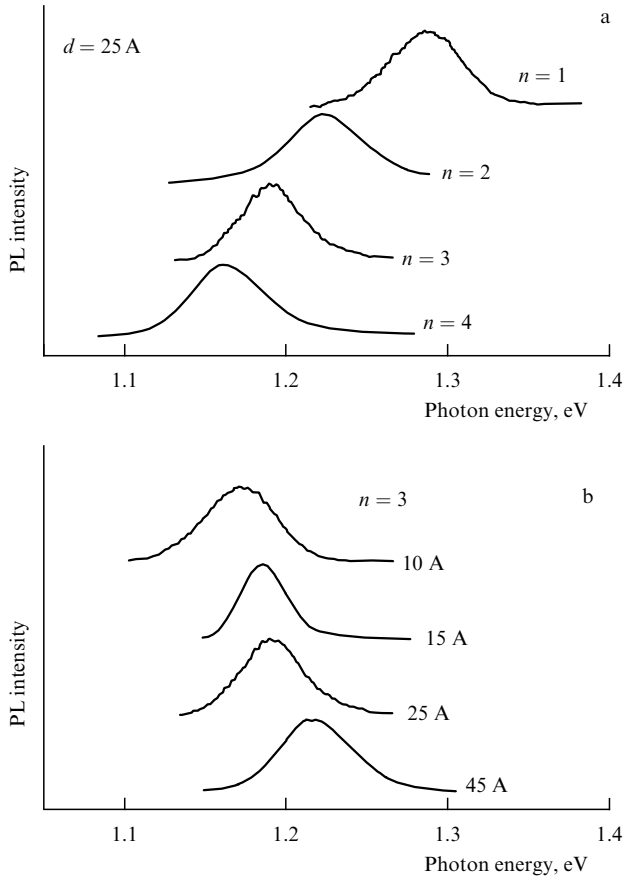

Figure 2. The photoluminescence (PL) of the tunnel-coupled quantum-dot structures studied at $T = 77$ K: (a) PL spectra of structures under one ($n = 1$), two, three, and four InAs deposition cycles producing layers of 5 A average thickness, which were separated by GaAs deposition layers of 25 A average thickness; (b) position of the PL line against the width of the GaAs layer for the $n = 3$ structure. Average InAs thickness is 5 A.

dots have shown a high characteristic temperature T_0 (as theoretically predicted in [18]) and the low threshold current density J_{th} ($T_0 = 425$ K, $J_{th} \approx 80$ A cm^{-2} in the temperature range 50 – 120 K) [17, 19]. This behaviour is consistent with the cathodoluminescence data, highly resolved in both energy and space, which suggest that the luminescence of an individual quantum dot gives rise to a supernarrow (less than 0.15 meV) line remaining unchanged under wide temperature variations and thus provides evidence for the formation of an *electronic* quantum dot [20]. At room temperature, however, the thermal escape of carriers from quantum dots brought about the deterioration of laser performance as well as shifting of the generation energy to shorter wavelengths (i.e. closer to the optical transition energy for the two-dimensional wetting layer). In order to increase the maximum gain and thus to improve the characteristics of quantum-dot lasers, arrays of InAs vertical-coupled quantum dots (VCQDs) in a GaAs matrix were used. In our case, such arrays yield a higher optical restriction coefficient and reduce the carriers' trapping, relaxation, and radiative recombination lifetimes, as well as increasing the gain and lowering the threshold current density.

The VCQD arrays were formed by a few successive deposition cycles, each producing an 1.7-monolayer-thick InAs layer and a 40 A GaAs layer. The schematic diagram of a VCQD is shown in Fig. 3a. Each dot consists of three vertical-coupled InAs parts separated by GaAs interlayers of 2 – 4 monolayer thickness. The upper and lower parts have lateral dimensions of order 170 A and 110 A, respectively. The electron and hole states in neighbouring islands are tunnel-coupled. The dots have square bases with [001]- and [010]-oriented sides and form a primitive square lattice in the plane of the substrate. At room temperature, the PL spectrum of such a structure exhibits an intensive line due to transitions between the electron and hole ground states in the tunnel-coupled dots [17].

Figure 3b is a schematic representation of the structure for laser studies. For the study of photoluminescence, the upper contact layer was chemically etched off. Figure 4 presents the electroluminescence spectrum of a VCQD laser system. Up to room temperature, the laser energy at low and moderate excitation densities corresponds to the peak of the PL spectrum. Thus, lasing occurs via the ground state of the VCQD. The temperature dependences of the threshold current density and lasing wavelength are given in Fig. 5a. In the temperature range 80 – 150 K, the threshold current density is essentially unchanged and equals 40 A/cm^2. The temperature dependence of the lasing wavelength follows that of the GaAs forbidden-gap energy. At observation temperatures above 180 K, a distinct rise in the threshold current density appears. This effect was observed previously in single-plane InAs quantum-dot lasers [17] at 80 K and is due to the thermal escape of carriers from the quantum dots. There is, however, no short-wave shift in laser energy and hence, up to room temperature, the lasing occurs via the dot-exciton ground state. In the case of a VCQD laser, the threshold current density at both 80 K and 300 K is much lower than for the laser with a single InAs quantum-dots layer. Moreover, the onset of the thermal escape of carriers into the wetting layer, and hence a sharp increase in T_0, shift upwards to

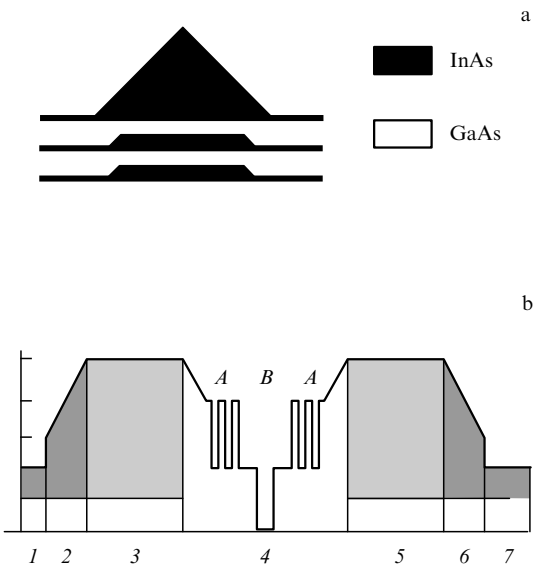

Figure 3. (a) Schematic diagram of vertical-coupled quantum dots (VCQDs). (b) Schematics of a VCQD laser structure. Region size, in μm: *1*, *2*, *6* — 0.2; *5* — 1.5; *4* — 0.4; *7* — 0.6. Impurity concentration (in 10^{18} cm^{-3}) and type: *1*, *2* — 4(Si); *3* — 2(Si); *5* — 0.7 (Be); *6*, *7* — 20(Be). In region *4*: *A* — 20 periods of the AlGaAs (20 A)/GaAs (10 A) superlattice; *B* — VCQDs inserted into a 800 A GaAs layer.

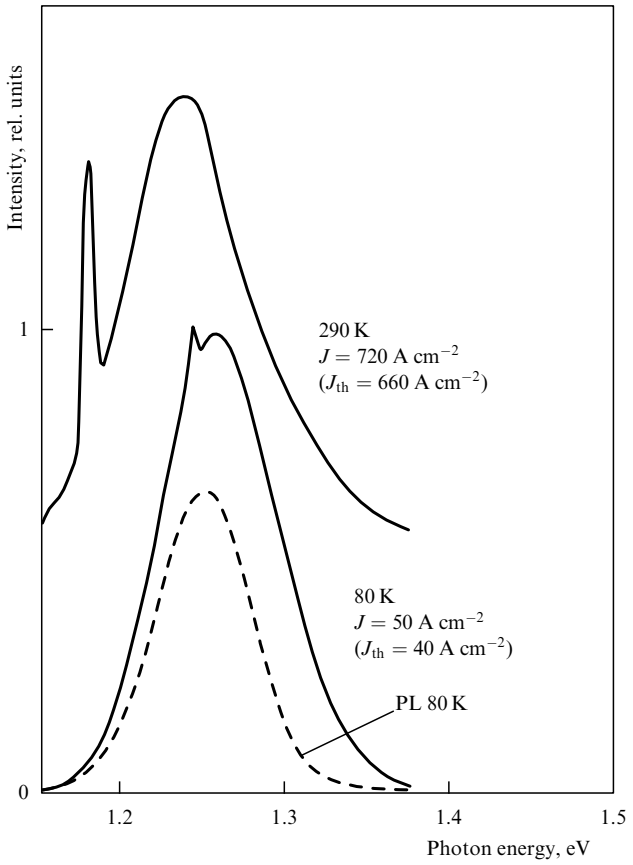

Figure 4. Electroluminescence spectra of a VCQD laser structure at 80 K and 290 K, and the photoluminescence spectrum at 80 K (dashed line) for the same structure with the upper emitter and contact layer chemically etched off.

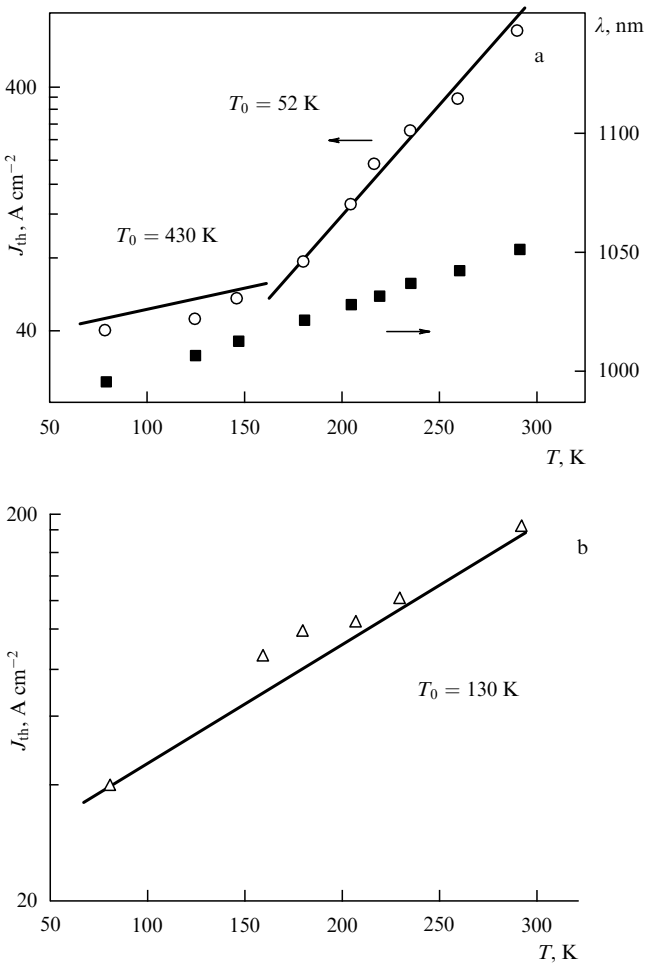

Figure 5. Variation of the threshold current density J_{th} and of the lasing wavelength λ with temperature for a laser with a VCQD (a) and singlequantumwell (b) active region.

180 K. Thus, the VCQD concept offers a significant improvement in laser performance and extends to higher temperatures the operation regime with the low threshold density and highly-temperature-stable threshold current. It is to be pointed out that the threshold current density for a laser structure with a single submonolayer-grown $In_{0.13}Ga_{0.87}As$ quantum well [10] has a temperature dependence describable by a characteristic temperature $T_0 = 130$ K over the entire range of 80 – 300 K (see Fig. 5b). Thus, the temperature behaviour of the threshold current density is radically different in the quantum-well and quantum-dots lasers, reflecting the difference in the form of the density of states for these two cases.

It is evident, then, that the use of vertical-coupled quantum dots enables lasing via the quantum-dots ground state up to room temperature and significantly extends the temperature stability range for the threshold current.

5. Conclusions

Bulk- and surface-stress effects may lead to the formation of ordered arrays of elastical-stressed three-dimensional islands in semiconducting matrices. The islands feature low dispersion in size and shape and are ordered, with respect to all three coordinates, into an artificial three-dimensional semiconducting crystal. The unique optical properties of such entities allow a qualitative improvement of the major parameters of semiconducting devices.

The support of the Russian Foundation for Basic Research, Volkswagen Foundation, International Science Foundation, and INTAS (Grant 94-1028) is gratefully acknowledged.

References

1. Kroemer H *Proc. IEE* **45** 1535 (1957)
2. Alferov Zh I, Kazarinov R F "Heterostructure-based semiconductor laser" *Avtorskoe Svidetel'stvo 27448 po Zayavke 950840 s Prioritetom ot 30 Marta 1963* (Certificate of Authorship 27448, priority application 950840, dated 30th March, 1963)
3. Kroemer H *Proc. IEE* **51** 1782 (1963)
4. Alferov Zh I et al. *Fiz. Tekh. Poluprovodn.* **1** 1579 (1967) [*Sov. Phys. Semicond.* (1967)]
5. Alferov Zh I et al. *Fiz. Tekh. Poluprovodn.* **3** 1328 (1969) [*Sov. Phys. Semicond.* (1969)]
6. Alferov Zh I et al. *Fiz. Tekh. Poluprovodn.* **4** 1826 (1970) [*Sov. Phys. Semicond.* (1970)]; Hayashi I et al. *Appl. Phys. Lett.* **17** 1803 (1970)
7. Aver'yanov M Yu et al. *Pis'ma Zh. Eksp. Teor. Fiz.* **48** 83 (1988) [*JETP Lett.* **48** 87 (1988)]
8. Ekimov A I, Onushchenko A A *Pis'ma Zh. Eksp. Teor. Fiz.* **40** 337 (1984) [*JETP Lett.* **40** 1136 (1984)]
9. Nötzel R et al. *Phys. Rev. Lett.* **67** 3812 (1992)
10. Wang P D et al. *Appl. Phys. Lett.* **64** 1526 (1994); Bressler Hill V et al. *Phys. Rev. B* **50** 8479 (1994)

11. Ledentsov N N, in *Proc. of the 22nd Int. Conf. on the Physics of Semiconductors in Vancouver, Canada, 1994* Vol. 3 (Ed. D J Lockwood) (Singapore: World Scientific, 1995) p. 1855
12. Shchukin V A et al. *Phys. Rev. Lett.* **75** 2968 (1995); Ledentsov N N, Grundmann M *Solid State Electronics* 1996 (in press)
13. Andreev A F *Sov. Phys. JETP* **53** 1063 (1981)
14. Marchenko V I *Sov. Phys. JETP* **54** 605 (1981)
15. Marchenko V I *Sov. Phys. JETP Lett.* **33** 381 (1981)
16. Shchukin V A et al. *Surf. Sci.* (1996) (in press)
17. Ledentsov N N et al. *Phys. Rev. Lett.* (1996) (in press)
18. Arakawa Y, Sakaki H *Appl. Phys. Lett.* **40** 939 (1982)
19. Kirstaedter N et al. *Electronics Lett.* **30** 1416 (1994)
20. Grundmann M et al. *Phys. Rev. Lett.* **74** 4043 (1995)

PACS numbers: 64.60.Ak, **71.30.+h**, **73.30.+y**

Percolation metal-dielectric transitions in two-dimensional electron systems

V T Dolgopolov

The energy spectrum of an ideal two-dimensional electron system in a static magnetic field consists of a set of δ-like peaks whose location on the energy scale corresponds to the cyclotron and spin splittings. A set of one-particle wave functions may be chosen to have each one of them describing a delocalised electronic state. In real systems a chaotic potential leads to the spreading of density-of-states peaks and produces localised electronic states on each of the quantum levels [1]. As long as the Fermi level is within the band of localised states, the dissipative conductivity is zero and its Hall counterpart is quantized: $\sigma_{xy} = n\,(e^2/h)$, where n is the number of bands of delocalised states below the Fermi level. The quantisation of σ_{xy} follows from the gauge invariance [2, 3] and must be exact in an infinite electron system at zero temperature.

Two points have received insufficient attention and thus deserve special mention. First, in an infinite two-dimensional electron system charge transfer, usually described by the σ_{xy} component, takes place under the Fermi level. Second, in a conventional integral-valued quantum Hall experiment [4], nondissipative charge transfer involves Fermi electrons in so-called edge channels [5 – 7]. Because of this latter circumstance, no information on the accuracy of σ_{xy} quantisation in real samples at finite temperatures can be derived from Hall bridge experiments.

Although a direct method of σ_{xy} measurement has long been known [2], its experimental realisation has only recently been performed [8 – 10]. Figure 1 reproduces one of the results of Ref. [9]. At minima of dissipative conductivity in Corbino sample geometries, a difference in potential between the outer and inside contacts is set up, due to the radial electron transfer caused by a change in the magnetic flux through the sample. A quantized value of σ_{xy} implies that an integer number of electrons is transferred through the sample under the flux change of one quantum. Hence, the sign of the measured voltage must depend on the magnetic field sweep direction, while its magnitude will be proportional to the magnetic field change with a coefficient dependent on the value of σ_{xy}. Since, in the experiments cited, the change in the number of electrons at the contacts exceeds their number in the sample, the reality of nondissipative transport under the Fermi level is unquestionable. Under the same conditions, the dissipative component of conductivity at sufficiently low temperatures is determined by the variable-step jumping of electrons with energies close to the Fermi energy.

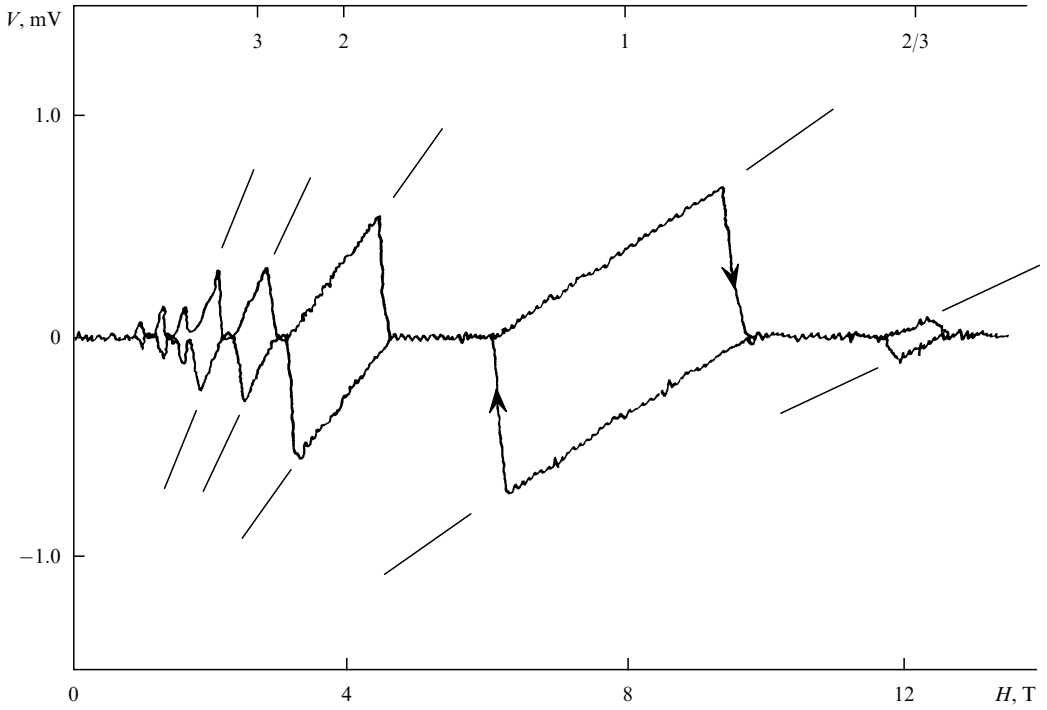

Figure 1. Experimental realisation of McLaughlin's mental experiment [9]. Ordinate represents the voltage drop across the plates of the capacitor short-circuiting the ring-shaped sample: heterostructure GaAs/AlGaAs at a temperature of 25 mK. Arrows display the magnetic field sweeping direction, straight lines show expected slopes for the quantized conductivity σ_{xy}.

In such a picture, electron transfer along the electric field will be of dielectric character independent of the number of delocalised bands below the Fermi level. As the magnetic field or the electron concentration is changed, the system will undergo the metal-dielectric transition twice at each of the quantum levels. The studies summarised below were aimed at determining the type of the corresponding transition and comparing the properties of dielectric phases which offered different numbers of delocalised states under the Fermi level.

The discussion above has shown that, from an investigation point of view, the most suitable samples are those of Corbino geometry, in which dissipative and nondissipative transport are completely decoupled. The measurements in [11] were made on samples fabricated from single GaAs/AlGaAs heterojunctions. As a means to control the concentration of two-dimensional electrons, part of the samples was provided with a ring gate separated from the outer and inner contacts by guarding rings of constant electron density. The volt-ampere characteristics of dielectric phases at minimum electron densities (no delocalised states under the Fermi level) and under integral-valued and fractional quantum Hall conditions $\nu = 2/3$, 1, 2 were examined. Direct current measurements using a Keithley 617 electrometer as a voltmeter were performed. The temperature ranged from 25 mK to 0.5 K, and magnetic fields varied up to 16.5 T. At the lowest temperature, the volt-ampere characteristics in all dielectric phases were nonlinear (see Fig. 2). The procedure shown in Fig. 2 was used to determine the threshold voltage. As seen from the figure, $U_c \propto (B - B_c)^2$ to a good accuracy. Similar I-V characteristics were seen in all dielectric phases studied. In the metal regions, the volt-ampere characteristics were linear. As the temperature rose, the nonlinearities were smoothed out. At the lowest temperature, the resistivity in the linear portion of the volt-ampere characteristic exhibits variable-step jumping conductivity, whereas at higher temperatures dissipative conductivity is activated. The temperature dependence of the resistivity in this temperature range enabled the activation energy E_a to be determined as a function of the magnetic field induction or the electron density. As seen in Fig. 2, the activation energy is a linear function of magnetic field and vanishes at the same point where U_c does. It is this point which we will treat as the metal-dielectric transition point. The validity of the assertion about the simultaneous vanishing of E_a and U_c was checked at the points marked in Fig. 3. Thus, experiment implies that the critical electric field F_c corresponding to the sharp increase of current in the dielectric phase is

$$F_c = \beta E_a^2. \tag{1}$$

The measured value of the coefficient β turned out to be the same within experimental accuracy for different dielectric phases.

For dielectric phases in the integral-valued quantum Hall regime, the relationship (1) is interpreted easily in terms of a percolation phase transition [12 – 14]. In fact, the linear variation of the activation energy with the filling factor implies a constant density of states near the transition energy. The dielectric phase contains clusters of electrons with overlapping wave functions. Conductance between the clusters proceeds via variable-step jumps. Near the percolation threshold, the characteristic cluster size $L(E)$ diverges with a critical exponent s like

$$L(E) = \beta_1^{-1} |E - E_c|^{-s}, \tag{2}$$

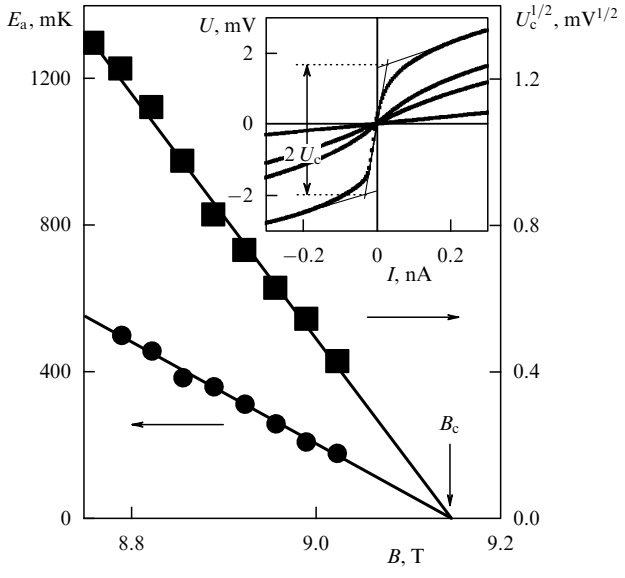

Figure 2. The magnetic field dependence of the activation energy E_a and of the critical voltage U_c in the $\sigma_{xy} = 2/3$ dielectric phase [11]. Insert shows volt-ampere characteristics in a magnetic field of 8.76 T at 25, 60, 74, and 114 mK. Also shown in the insert is the procedure of determining the value of U_c. All other investigated phases exhibit a stronger nonlinearity.

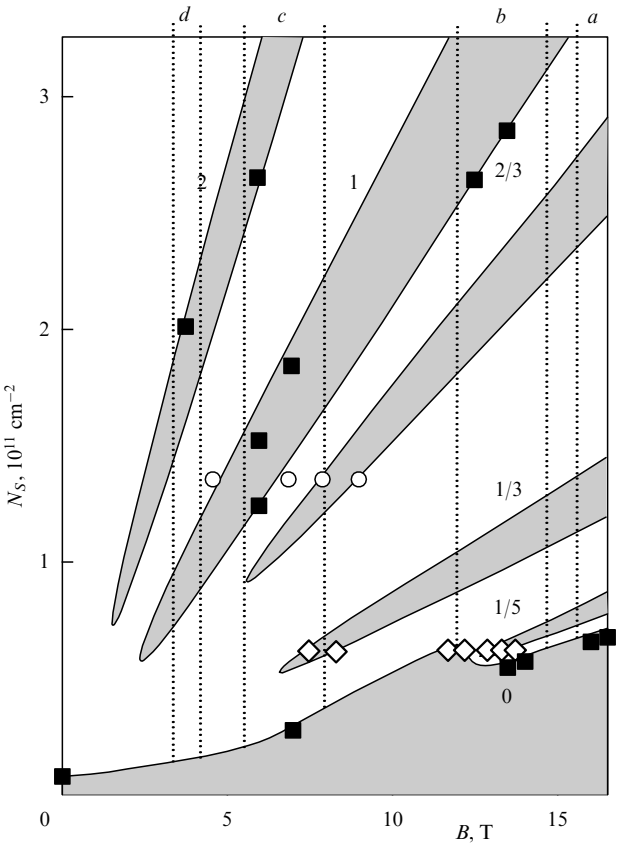

Figure 3. Phase diagram for metal-dielectric transitions in the (N_S, B) plane, from GaAs/AlGaAs heterostructure measurements [11]. Numbers indicate the Hall conductivity in units of e^2/h for various dielectric phases.

where β_1 characterises the random potential. In weak electric fields, clusters are equipotential, thus reducing the energy interval, which ranges up to mobility threshold, by $eFL(E_F)$. In the critical electric field

$$F_c = \frac{E_a}{eL(E_F)} = e^{-1}\beta_1 E_a^{s+1} \tag{3}$$

we reach the mobility threshold and, in accordance with experiment, the current increases sharply. It is readily seen that Eqs (1) and (3) are identical for $\beta_1 = e\beta$ and a critical exponent $s = 1$, which is close to the theoretical value $s = 1.3$ expected from the classical percolation. Hence, the experimental results can be interpreted as due to the electric-field-induced electron delocalisation of classical percolation type. Based on the experimental data involved, a phase diagram in the (B, N_S) plane can be constructed (see Fig. 3).

Similar experimental findings were obtained on high-mobility silicon MOS structures [13, 14]. Since these measurements were made on Hall bridges [15], U_c was taken to be the Hall voltage at which longitudinal resistivity starts to grow. The volt-ampere recalculation procedure is described in detail in Ref. [14]. As an illustration, Fig. 4 presents the dependence of the critical voltage on the electron density in a fixed magnetic field. Here, too, a direct proportionality between $U_c^{1/2}$ and the electron concentration is observed near each transition point. The corresponding straight lines extrapolate to the same electron concentrations at the transition points, when they are compared with results obtained from extrapolating the activation energy to zero. A (B, N_S)-plane phase diagram for a two-dimensional electron gas in a silicon MIS structure is shown in Fig. 5.

It should be noted that entirely analogous relations have been obtained for a two-dimensional hole gas in Ge/SiGe heterostructures [17], which indicates the universality of the percolation nature of the transition.

The results cited above have been confirmed, directly or otherwise, in a number of experimental studies. Time-resolved optical studies may show what fraction of the area is occupied by the metal or dielectric phase in the transition to the dielectric state with $\sigma_{xy} = 0$ [18, 19]. In all such measurements, the transition to the dielectric state is found to occur at exactly the filling factor for which one of the phases occupies 50% of the area — the way the percolation transition in a two-dimensional system is expected to proceed [20].

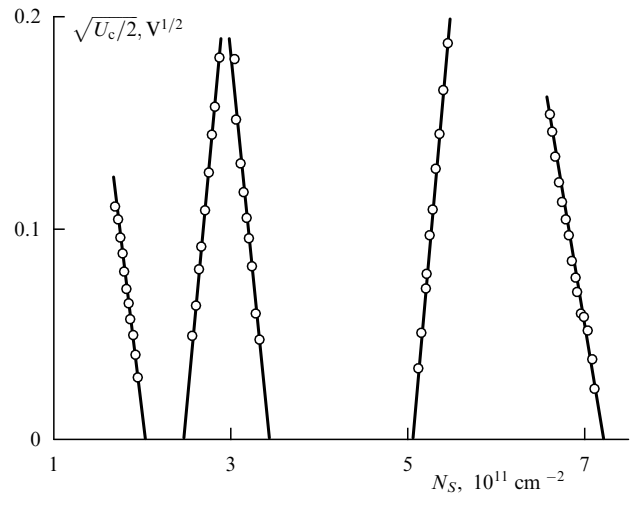

Figure 4. Critical voltage against electron concentration near the phase boundaries corresponding to $\sigma_{xy}h/e^2 = 0, 1, 2$ in a magnetic field of 12 T: silicon MOS structure at 25 mK [14].

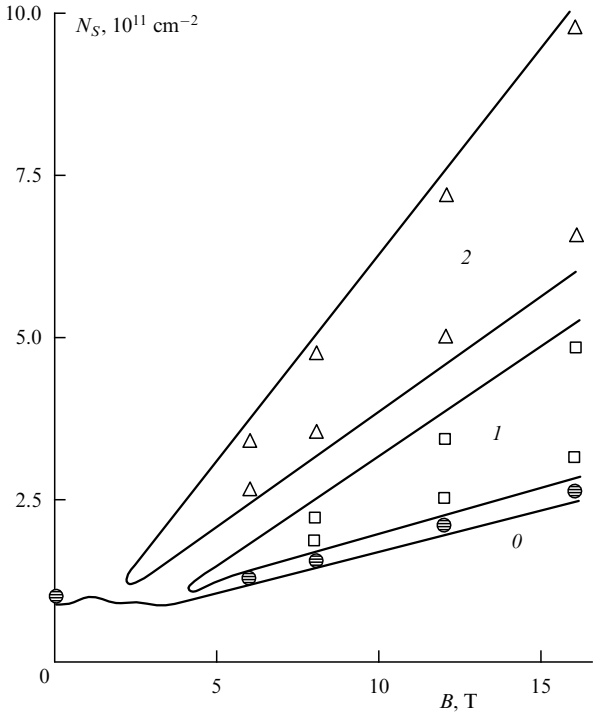

Figure 5. Phase diagram in the (N_S, B) plane for a silicon MOS structure: from a fixed value of σ_{xx}^{-1} (solid lines), and from activation energy vanishing points (symbols) [14].

Phase diagrams in the (N_S, B) plane have been reproduced in [21, 22] by using a procedure which is somewhat different from that outlined above. Furthermore, in Ref. [22] an experimental version of the global phase diagram is constructed which describes all the experimental results that are currently available.

The present work is supported by the 'Solid State Nanostructure Physics' Programme, by RFBR through Grant No. 93-02-02304, and by the Volkswagen Foundation (Grant No. I/68553).

References

1. *The Quantum Hall Effect* (Eds R E Prange, S M Girvin) (New York, Berlin, Heidelberg, London, Paris, Tokyo: Springer-Verlag, 1987)
2. Laughlin R B *Phys. Rev. B* **23** 5632 (1981)
3. Halperin B I *Phys. Rev. B* **25** 2185 (1982)
4. v. Klitzing K, Dorda G, Pepper M *Phys. Rev. Lett.* **45** 494 (1980)
5. Büttiker M *Phys. Rev. B* **38** 9375 (1988)
6. Shklovskii D B, Shklovskii B I, Glazman L I *Phys. Rev. B* **46** 4026 (1992)
7. Haug R J *Semicond. Sci. Technol.* **8** 131 (1993)
8. Dolgopolov V T, Zhitenev N B, Shashkin A A *Pis'ma Zh. Eksp. Teor. Fiz.* **52** 826 (1990) [*JETP Lett.* **52** 196 (1990)]
9. Dolgopolov V T et al. *Phys. Rev. B* **46** 12560 (1992)
10. Dolgopolov V T et al. *Phys. Rev. B* **48** 8480 (1993)
11. Shashkin A A et al. *Phys. Rev. Lett.* **73** 3141 (1994)
12. Shklovskii B I *Fiz. Tekhn. Poluprovodnikov* **13** 93 (1979)
13. Dolgopolov V T et al. *Phys. Rev. B* **46** 13303 (1992)

14. Shashkin A A, Dolgopolov V T, Kravchenko S V *Phys. Rev. B* **49** 14486 (1994)
15. A study on the properties of the $\sigma_{xy} = 0$ dielectric phase in weak magnetic fields using silicon MIS Hall bridges of equivalent or higher quality was conducted in a number of papers by V M Pudalov with coworkers (see, e. g., Ref. [16])
16. Kravchenko S V, Furneaux J E, Pudalov V M *Phys. Rev. B* **49** 2250 (1994); Pudalov V M, D'Iorio M, Campbell J W *Surf. Sci.* **305** 107 (1994)
17. Dolgopolov V T *Pis'ma Zh. Eksp. Teor. Fiz.* **62** 152 (1995) [*JETP Lett.* **62** 168 (1995)]
18. Kukushkin I V, Timofeev V B *Usp. Fiz. Nauk* **163** (7)1 (1993)[*Phys. Usp.* **36** 549 (1993)]
19. Kulik S P et al. *Phys. Rev. B* **51** 3362 (1995)
20. Shklovskii B I, Efros A L *Electronic Properties of Doped Semiconductors* (New York: Springer-Verlag, 1984)
21. Glozman I, Johnson C E, Jiang H W *Phys. Rev. Lett.* **74** 594 (1995)
22. Kravchenko S V et al. *Phys. Rev. Lett.* **51** 7038 (1995)

PACS numbers: 73.20.Dx, **73.90.+f**, 78.66.Fd

Nonlinear optical properties of semiconducting quantum wires and dots

V S Dneprovskiĭ

1. Introduction

In recent years much attention has been devoted to the unusual properties of semiconducting nanostructures with carrier motion restricted in two or three directions (quasi-one-dimensional quantum wires and quasi-zero-dimensional quantum dots). Effects of energy dimensional quantisation in these nanostructures are more important than in their quasi-two-dimensional counterparts. The energy gaps between electronic states increase, and the density of states, which is step-like for two dimensions, becomes discrete (forms a set of separate peaks) in an ideal quasi-one-dimensional and zero-dimensional structures. The effect of quantum restrictions in two or three directions must lead to narrower light amplification spectrum; to greater differential gain [1]; to increased exciton binding energy and magnified exciton lasing [2]; and, finally, to enhanced optical nonlinearities [3]. Quasi-zero-dimensional and one-dimensional structures hold promise as low-threshold laser active media for high-temperature performance; and also as efficient, fast optical switches with low expenditure of energy. Quasi-one-dimensional structures with high-movable carriers in quantum wires may pave the way to next-generation transistors.

This paper presents the results of a study on the nonlinear optical properties† of semiconducting quantum wires and dots by ps-resolution laser saturation spectroscopy techniques. Samples with CdSe quantum dots [6] and GaAs [7], CdSe, or CdS quantum wires, as well as porous silicon [8] exhibit clarified bands in nonlinear transmission spectra obtained at different times after excitation by an ultrashort laser pulse. It is shown that the physical process leading to strong optical nonlinearities in semiconducting quantum wires and dots constitutes the saturation of optical transitions between the dimensional quantisation levels during excitation of high-density nonequilibrium carriers. It is also shown that nonlinear absorption spectra are discrete even if a sample containing variously shaped and widely different in size semiconducting nanostructures, exhibits no features in linear absorption spectra to indicate the discrete nature of the optical transitions. This is presumably due to the nonuniform line broadening being partially suppressed during the resonance laser excitation of the ensemble of nanostructures of a given size (with identical optical transition spectra).

Amplification and lasing for the optical transitions between the lowest dimensional quantisation levels in semiconducting quantum dots (glass-matrix CdSe nanocrystal structure) have been detected [9]. The magnitudes and relaxation times of nonlinear susceptibilities of samples with semiconducting wires and dots were measured as well.

†The subject of the study is the so-called strong (resonance) dynamic nonlinearities, i.e. the nonlinear change of the optical properties of nanostructures absorbing(!) laser radiation [4]. Unlike inertialess 'classical' nonlinearities in transparent media, which are caused by the nonlinear polarisability of electrons in an intense light field, the relaxation time of a strong dynamic nonlinearity relates to recombination of nonequilibrium electrons or other quasiparticles. A strong optical nonlinearity due to the saturation of an optical transition was first discovered by S I Vavilov in 1926 in an experiment on the nonlinear absorption of uranium glass under resonance excitation [5].

2. Nonlinear absorption of GaAs and CdSe quantum wires

There are several ways of fabricating semiconducting quantum wires by combining molecular-beam and liquid epitaxy techniques with surface etching, previous fixed-angle cleaving of the substrate surface, etc. [10]. These methods, however, do not yield sample sizes necessary for measuring linear and nonlinear absorption spectra. Recently, a new procedure for obtaining semiconducting quantum wires in a transparent dielectric matrix has been introduced [11], in which a melted semiconducting material (GaAs, CdSe, etc.) is injected into hollow cylindrical chrysotile-asbestos channels about 6 nm in diameter. A sample is a regular close-packed structure of parallel chrysotile-asbestos 30-nm-diameter nanotubes filled with ultrathin crystalline wires of GaAs or CdSe. The size of the samples and the concentration of nanostructures enable the spectra of both linear and nonlinear absorption to be measured. In measuring nonlinear absorption spectra, the probe method of Ref. [6] was employed: the sample excited by an ultrashort laser pulse is probed by an ultrashort wide-spectrum ('white' light) pulse. Using an optical delay line has made it possible to detect the transmission spectra of the samples at various times after the excitation.

In Fig. 1, the linear absorption spectrum and that of differential transmission $DT(\lambda)$ ($(DT(\lambda) = [T(\lambda) - T_0(\lambda)]/T_0(\lambda)$, where $T(\lambda)$, $T_0(\lambda)$ are the spectra of an excited and an unexcited sample) are presented. The latter exhibits two clearly distinct clarified bands having maxima at 1.8 and 2.2 eV and coinciding with the linear absorption bands. The induced clarification disappears after 50 ps.

In bulk semiconductors various competing nonlinear processes coexist depending on the conditions, such as the Burstein–Moss dynamical saturation, forbidden-gap energy renormalisation (narrowing) at high concentrations of nonequilibrium carriers, clarification and broadening of the exciton absorption line for collectively interacting or free-carrier-screened excitons, etc. [13]. In semiconducting quantum dots and wires, only one nonlinear absorption process, the saturation of the optical transition by non-equilibrium carriers, manifests itself in the spectral region of the lowest quantum transition [3].

The appearance of clarified bands (Fig. 1) can be attributable to the saturation of discrete optical transitions resulting from dimensional quantisation in quantum wires. In

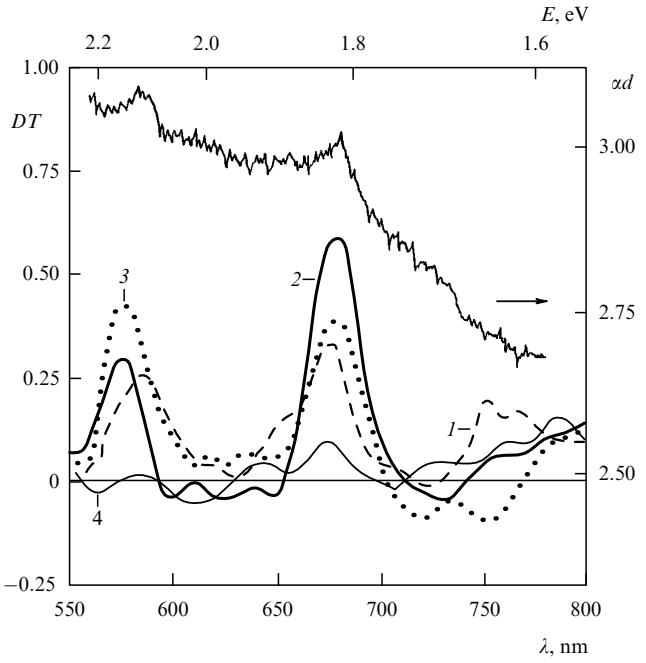

Figure 1. Linear absorption and differential transmission spectra of GaAs quantum wires in chrysotile-asbestos nanotubes, at various delays between the exciting and probe pulses: *1*— (–15) ps (probe pulse ahead of pumping); *2* — 0 ps; *3* — 20 ps; *4* — 50 ps.

the effective mass approximation, and assuming an infinite cylindrical potential well along with no Coulomb interaction between the carriers, the transition energies between the dimensional quantisation levels of the conduction band electrons and the holes of the corresponding valence bands take the form [13]

$$E_i = E_g^i + \frac{X_{01}^2 \hbar^2}{2\mu_i \rho^2} ,$$

where E_g^i is the forbidden-gap energy (index i denoting the valence band); $X_{01} \approx 2.4$; μ is the reduced effective mass, ρ is the wire radius. From this expression, it can be shown that for a 6-nm-diameter quantum wire the 1.8-eV band corresponds to the transition between the first heavy-hole and the lowest electron dimensional quantisation levels, whereas the 2.2-eV band, to that for the holes of the spin-orbit-split valence band and the lowest electron level. Knowing the magnitude and relaxation time of the detected spectral clarification allows one to estimate the third-order nonlinear susceptibility of the sample: $\mathrm{Im}\,\chi^{(3)} = -4 \times 10^{-8}$ CGS. The CdSe containing chrysotile-asbestos samples display a clarified band corresponding to the lowest transition due to the dimensional quantisation in 6-nm-diameter quantum wires.

3. Strong optical nonlinearities in porous silicon

Porous silicon has received particular attention owing to its possible application in optoelectronics as a material effectively luminescing in the visible spectrum [14]. One of the proposed mechanisms for this luminescence involves the rearrangement of appropriate energy spectrum as a result of the dimensional quantisation in the quantum wires and dots that form in the material. However, the discrete spectrum of optical transitions has so far evaded detection, presumably because of the wide spread in size and the variation in shape of the nanostructures. The method of nonlinear laser saturation spectroscopy has permitted measurement of nonlinear absorption in porous silicon layers cleft off from the silicon substrate. It was also possible to detect discrete clarified bands relevant to the saturation of optical transitions between the dimensional quantisation levels in quantum wires and dots, and to determine the energy spectrum of the material [8].

Figure 2 shows the linear absorption and differential transmission spectra of one of the porous silicon samples. Whereas the former is featureless (smooth), in the latter discrete clarified bands are clearly seen. Their energy position suggests the presence of two types of nanostructure (quantum wires and dots) [8], and leads to an estimate of their average size (diameter) as of about 3 nm and 4 nm, respectively. Measurements with electron and scanning-tunnelling microscopy have independently confirmed the existence of quantum wires and dots of proper size in porous silicon samples. The measured value of the linear susceptibility amounted to $\mathrm{Im}\,\chi^{(3)} \approx -0.2 \times 10^{-8}$ CGS.

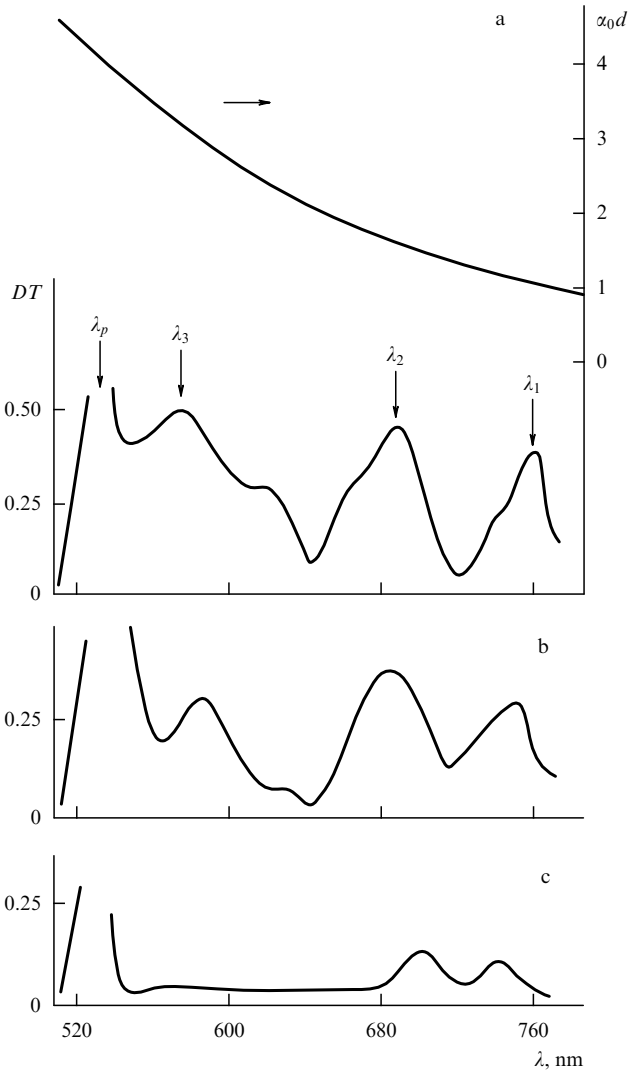

Figure 2. Linear absorption and differential transmission spectra of porous silicon (300 K). The differential transmission spectra are obtained at various times after the excitation: (a) at the instant of excitation; (b) 20 ps after the excitation; (c) 27 ps after the excitation.

4. Amplification and lasing in samples with CdSe quantum dots

The measurement of the differential transmission spectra in CdSe quantum-dot nanostructures in a glass matrix enabled amplification (absorption coefficient $\alpha < 0$) at the lowest optical transition frequencies to be detected [9]. To achieve lasing, a Fabry–Perot resonator about 1 mm long was manufactured, with dielectric mirrors transparent to the pumping wavelength (532 nm) and with reflection coefficients of 100% and 95% at the 650 nm wavelength corresponding to the lowest optical transition in CdSe quantum dots with an average radius of 5 – 6 nm. With an increase in the pumping energy (for excitation by an ultrashort, second-harmonic, mode-locking Nd:YAG laser pulse), a transition from spontaneous to stimulated emission was detected [9].

5. Optical and nonlinear optical properties of CdS nanostructures

A new method, suggested by V A Karavanskiĭ, enables the manufacture of semiconducting nanostructures of various (!) size on crystallising the semiconductor by layer-to-layer chemisorption in the hollow channels of molecular filters (mica bombarded by accelerator ions). The channel diameter, and hence the size of the nanostructure, can be changed by varying the kind and energy of the ions. The resulting samples, containing quantum wires with average diameter of about 7 nm, display features ('hills') in the linear absorption spectra, and clarified bands in differential transmission spectra, both the features and the bands corresponding to the optical transitions between the dimensional quantisation levels of the A and C valence band holes and the lowest dimensional quantisation level of the conduction band electrons. The relaxation time of the induced clarification comes to about 100 ps.

6. Conclusions

A strong and fast optical nonlinearity is detected in samples with GaAs, CdSe, and CdS quantum wires, in those with CdSe quantum dots, and in porous silicon. The saturation of optical transitions between the dimensional quantisation levels in quantum wires and dots constitutes the main physical process responsible for the nonlinearity.

The work is supported by the International Science Foundation (Grants M5D000 and M5D300) and the 'Solid State Nanostructure Physics' Programme (project 1-034).

References

1. Arakawa Y, Yariv A *IEEE J. Quantum Electron.* **22** 1887 (1986)
2. Weigscheider W et al. *Phys. Rev. Lett.* **71** 4071 (1993)
3. Schmitt–Rink S, Miller D A B, Chemla D S *Phys. Rev. B* **35** 8113 (1987)
4. Butcher P N, Cotter D *The Elements of Nonlinear Optics* (Cambridge: University Press, 1990)
5. Vavilov S I *Mikrostruktura Sveta* (Light Microstructure) (Moscow: Akad. Nauk SSSR, 1950)
6. Vandyshev Yu V, Dneprovskiĭ V S, Klimov V I *Zh. Eksp. Teor. Fiz.* **101** 270 (1992) [*Sov. Phys. JETP* **74** 144 (1992)]; Vandyshev Yu V, Dneprovskiĭ V S, Klimov V I *Pis'ma Zh. Eksp. Teor. Fiz.* **53** 301 (1991) [*JETP Letters* **53** 314 (1991)]
7. Gushchina N V et al. *Pis'ma Zh. Eksp. Teor. Fiz.* **61** 491 (1995) [*JETP Letters* **61** 507 (1995)]; Dneprovskiĭ V S et al. *Phys. Lett. A* **204** 59 (1995)
8. Dneprovskiĭ V S et al. *Pis'ma Zh. Eksp. Teor. Fiz.* **57** 394 (1993) [*JETP Letters* **57** 406 (1993)]; Dneprovskiĭ V S et al. *Superlattices and Microstr.* **17** 41 (1995); Dneprovskiĭ V S et al. *Phys. Status Solidi B* **188** 297 (1995)
9. Dneprovskiĭ V S et al. *Solid State Commun.* **81** 227 (1992); Vandyshev Yu V et al. *Pis'ma Zh. Eksp. Teor. Fiz.* **54** 441 (1991) [*JETP Letters* **54** 442 (1991)]
10. Sundaram M S et al. *Science* **254** 1326 (1991)
11. Poborchiĭ V V, Ivanova M S, Salamatina I A *Superlattices and Microstr.* **16** 133 (1994)
12. *Nonlinear Photonics* (Eds H M Gibbs, G Khitrova, N Peyghambarian) (Berlin: Springer-Verlag, 1990)
13. Zarem H, Vahala K, Yariv A *IEEE J. Quantum Electron.* **25** 705 (1989)
14. Canham L T *Appl. Phys. Lett.* **57** 1046 (1990)

PACS numbers: 73.20.Dx, **73.25.+i**, 75.30.–m

Quasi-one-dimensional conductors with a charge density wave

S N Artemenko, A F Volkov, S V Zaitsev-Zotov

1. Introduction

As the temperature is lowered, a Peierls transition occurs in quasi-one-dimensional conductors, giving rise to a superlattice, i.e. either a charge density (CDW) or spin density (SDW) wave whose period is half the Fermi electron wavelength in the metal. The properties of CDW- and SDW-containing materials are very similar and reviewed in a recent book [1]. This paper is limited to CDW conductors, and we shall start by discussing their basic properties briefly.

The Peierls transition temperature is typically $T_P \approx 100$ – 200 K. For example, in TaS_3 this is 220 K, in blue bronze $K_{0.3}MoO_3$, 180 K, and in $(NbSe_4)_{10/3}I$, 280 K. In fact, the CDW makes an electron crystal analogous to the Wigner one. The formation of a CDW produces an energy gap 2Δ at the Fermi surface, bringing the conductor either into a semimetal state (as $NbSe_3$) or into a semiconducting state (as other quasi-one-dimensional CDW conductors). In the Peierls state, one-electron excitations (electrons and holes) coexist with the deformable mobile electron crystal, the CDW. That the CDW can move follows from the translational invariance of the CDW position in a perfect crystal. The translational invariance, however, is violated either by the presence of impurities or by the commensurability of the crystal and CDW periods (CDW pinning). As a result, the CDW must overcome the energy barrier in order to be able to move. Therefore, the CDW begins to slide if the crystal is subject to an electric field E exceeding the threshold value E_T, the latter depending on the impurity concentration and the temperature. For $E > E_T$, the CDW can move and contribute to the current, with the result that the crystal conductivity rises by several orders of magnitude as the electric field is increased.

For $E < E_T$, the CDW cannot move as a whole and the conductivity of the quasi-one-dimensional conductor is determined by one-electron excitations. This makes the material similar to an ordinary semiconductor except that the deformation of the CDW (in an electric field, for example) changes the electron and hole concentrations. As a result, the CDW perturbations affect the conductivity in the fields weaker the threshold field as well. The contribution of the CDW to the conductivity is not limited to its motion as a whole, but may also be caused by the motion of nonlinear CDW excitations, i.e. the electron crystal defects like solitons and dislocations.

To date, the properties of CDW conductors are by and large well understood for relatively high temperatures $T \geqslant T_P/3$ (see reviews in Ref. [2]), at which the effects cited above are quite reproducible and fairly well described in terms of the CDW viewed as an elastic medium whose interaction with impurities is described by the weak (collective) pinning theory [3]. The major features of high-temperature CDW-involving transport phenomena are understood not only at the phenomenological level but also within the framework of microscopically derived kinetic equations [4].

The properties of the CDW at lower temperatures are understood much less than at high temperatures. The wide spread in sample parameters in this region indicates the importance of defects. As the temperature is lowered, the activation energy for the linear in-chain conductivity decreases, whereas that for the transverse conductivity remains unchanged [5], and there is also a sharp drop in thermo-emf, which even changes sign in some substances, such as TaS_3 [6] and $(NbSe_4)_{10/3}I$ [7]. Moreover, there appears a sharp growth of the threshold field, and the nonlinear conductivity activation energy starts to be electric field dependent. At extremely low temperatures (for example, below 20 K for TaS_3), effects attributable to the glass properties of the CDW occur. These are, in particular, a peak in the low-frequency dielectric permittivity [8 – 10] and a decelerated relaxation of the electric-field response. Whether the transformation to the glass state provides a phase transition is as yet not altogether clear. Along with evidence in favour of this, alternative explanations exist, which invoke the temperature dependence of the screening length of inhomogeneous CDW perturbations in the field for pinning impurities [11], or the transition from weak to strong pinning with lowering temperature [12].

Below we shall take a closer look at some recent results concerning the low-temperature region.

2. Screening and local CDW defects (solitons)

Since a CDW phase gradient implies a perturbation of the CDW charge density, nonhomogeneous phase perturbations dominate the kinetic properties of quasi-one-dimensional conductors. This is true of both perturbations due to pinning centres (contacts, and other inhomogeneities) and nonlinear CDW perturbations, which may act as quasiparticles. It has been suggested [5, 13, 14] that current carriers in CDW conductors may be represented by phase solitons, i.e. phase perturbations in which the phase of one of the chains changes by 2π. Such solitons may be considered as vacancies or as extra sites in the electron crystal. The energy of a phase soliton is determined by the coupling between conducting chains, which is much less than the Peierls gap Δ, so that as the temperature is lowered, the electrons and holes are expected to be frozen out and solitons may become dominant current carriers in a state wherein the CDW as a whole is at rest.

We have shown earlier [15, 16] that the results pertaining to local CDW perturbations need to be revised, since nonlinear screening effects, usually left out of account, make screening by one-electron excitations effective down to the lowest temperatures involved. In particular, the defects of the electron crystal (solitons) and those of the crystal (impurities, pinning centres) lead to a strong bend of the energy bands, so that the Fermi level may even fall into the energy range of allowed one-electron states. The electrons in the metal islands thus formed around the defects must affect the kinetic and thermodynamic properties of CDWs at low temperatures: a reason, in particular, for a strong rise in the soliton energy.

The problem of spatial CDW perturbations is treated by using the Green's function equations [4], which are first extended to large interchain CDW phase differences via the lattice-site chain-number Wannier representation and then integrated over the momentum component along the conducting chains. For simplicity we have used the electron-chain tight-binding approximation, in which the spectrum perpendicular to the chains is $\epsilon_\perp = 2t_\perp(\cos ap_y + \cos ap_z)$, $t_\perp \ll \Delta$. In the equilibrium case it suffices to find the retarded, g^R, and the advanced, g^A, Green's functions, which are two-index matrices with one index labelling the $+p_F$ and $-p_F$ sheets of the Fermi surface in the quasi-one-dimensional conductor under study, and the other being n, the number of the chain. The solutions have two characteristic length scales along the chains: a small one, on the order of the correlation length $\xi = \hbar v_F/\Delta$, and a macroscopic one, which is determined by the large decay lengths pertaining to phase perturbations and the electric potential Φ. The smooth solutions relevant to the latter scale can be found quasiclassically and, provided the momentum scattering time ($\tau \ll \Delta/t_\perp^2$) is sufficiently small, these equations even hold when the departure of the local chemical potential μ from its equilibrium centre-of-the-forbidden-band position is large enough to reach the edge of the energy gap. Application of the quasiclassical approximation led to equations coupling phase gradients with the electric field strength and the chemical potential shift (the latter equal to the shift of the electric potential in equilibrium); and made it possible to calculate the charge density which is substituted in the Poisson's equation. As a result, a system of equations relating phases and potentials at different chains was obtained. In the limit $|\mu| \ll \Delta$, these equations reduce to the conventional ones [14] describing local phase perturbation to linear order in potential. We have solved the resulting equations both numerically [16] and analytically [15] (for a simplified model interaction). Although the results depended quantitatively on the concrete chain arrangement, their qualitative form turned out to be the same for different models.

The main calculated results may be outlined as follows. At zero temperature, the in-chain phase-perturbation decay length equals $\hbar v_F/(t_\perp\sqrt{\zeta})$, and the off-centre shift of the chemical potential μ (due to the phase being perturbed up to the order of π at one of the conducting chains) is of order $t_\perp/\sqrt{\zeta}$, where $\zeta = 1/(\kappa d)^2 \equiv \hbar v_F/8e^2$ describes the ratio of the Fermi energy to the Coulomb energy. Here κ is the inverse Thomas–Fermi screening radius in the metal state, and d is the conducting chain separation. For typical values of $v_F = 2 \times 10^7\,\mathrm{cm}^{-1}$, $\zeta \approx 10^{-2}$. The small value of the parameter ζ leads to large shifts $\mu \sim \Delta$ and to the large phase-soliton energy. Thus, at $T = 0$ and provided $\zeta\Delta^2/t_\perp^2 < b$ (where $b = O(1)$ depends on the chain arrangement and the interchain interaction energy range), the chemical potential near the strong pinning centres (the phase on which being specified by the impurity itself) and at the phase-soliton centres reaches the Peierls gap edge and thus gives rise to a metal island. According to estimates, this condition is expected to be fulfilled in typical CDW conductors.

At temperatures $T > T_M = O(t_\perp^{4/3}/\Delta^{1/3})$, the screening by electrons thermally excited around the gap becomes rather effective, and the shift in μ does not reach Δ. As the temperature is further increased, the screening of the charge produced by the CDW phase perturbation becomes increas-

ingly effective and the shift in μ, still less. As this takes place, the soliton energy decreases with a rise in temperature and depends on the sign of the soliton charge, being less when the sign is opposite to that of the principal one-electron charge carriers. This means that when the one-electron conduction gives way to the soliton picture (or, if the CDW creep conduction sets in, to a mechanism involving soliton motion between pinning centres [17]), a change in the sign of principal charge carriers should occur, a fact which may account for the change in the sign of thermo-emf observed as the temperature is lowered.

3. CDW quantum creep

Thin TaS_3 layers with a cross section of order 10^{-1} μm^2 exhibit an unusual temperature dependence of the nonlinear conductivity indicating the appearance of quantum effects in the CDW motion [18]. At temperatures $T > 10$ K, the properties of such samples differ little from those of ordinary size. Thus, as the temperature is lowered below 100 K, the threshold field E_T for the onset of CDW sliding becomes rapidly higher and is much above 100 V/cm at $T < 50$ K (see Fig. 1). In so doing the volt-ampere characteristics exhibit an additional nonlinearity at $E < E_T$. At $T > 20$ K, the temperature-dependent nonlinear current (Fig. 2) are of an activated form, $\ln I \propto 1/T$, with an activation energy $W = \mathrm{d}\ln I/\mathrm{d}(1/T)$ dependent on the electric field strength.

In the low-temperature region, however, the nonlinear conductivity of thin samples behaves differently from that for ordinary sizes. Below 10 K, the temperature dependence of the CDW nonlinear current virtually disappears (Fig. 2), and the volt-ampere characteristic itself rapidly approaches the limiting curve of the form

$$I \propto \exp\left[-\left(\frac{E_0}{E}\right)^2\right] \tag{1}$$

(see insert in Fig 1), where $E_0 \sim 10^3$ V cm^{-1}. It turns out that as $T \to 0$, the nonlinear current tends to a constant *nonzero* quantity (see insert in Fig. 2). This signals the appearance of an additional channel for overcoming the energy barrier inhibiting the CDW motion. Since the probability for overcoming the barrier (whose measure is the CDW current) proves finite at $T = 0$, it is natural to assume that barriers are overcome by tunnelling.

Thin samples offer a characteristically high noise level in the region of nonlinear conductivity at low temperatures. A detailed noise study [18] showed that, for example, in a sample with a cross section of 10^{-2} μm^2, the current is carried by small groups of electrons (about 10^6 in number) coming irregularly in time, the current being close to zero between the arrival of individual portions. This implies that we are dealing with a collective effect and that the current is carried via a certain random process. Most likely, this is a creep (spatially nonuniform CDW motion in the pinning force field) which is thermally activated at $T > 10$ K and is of quantum nature at lower temperatures. A further important

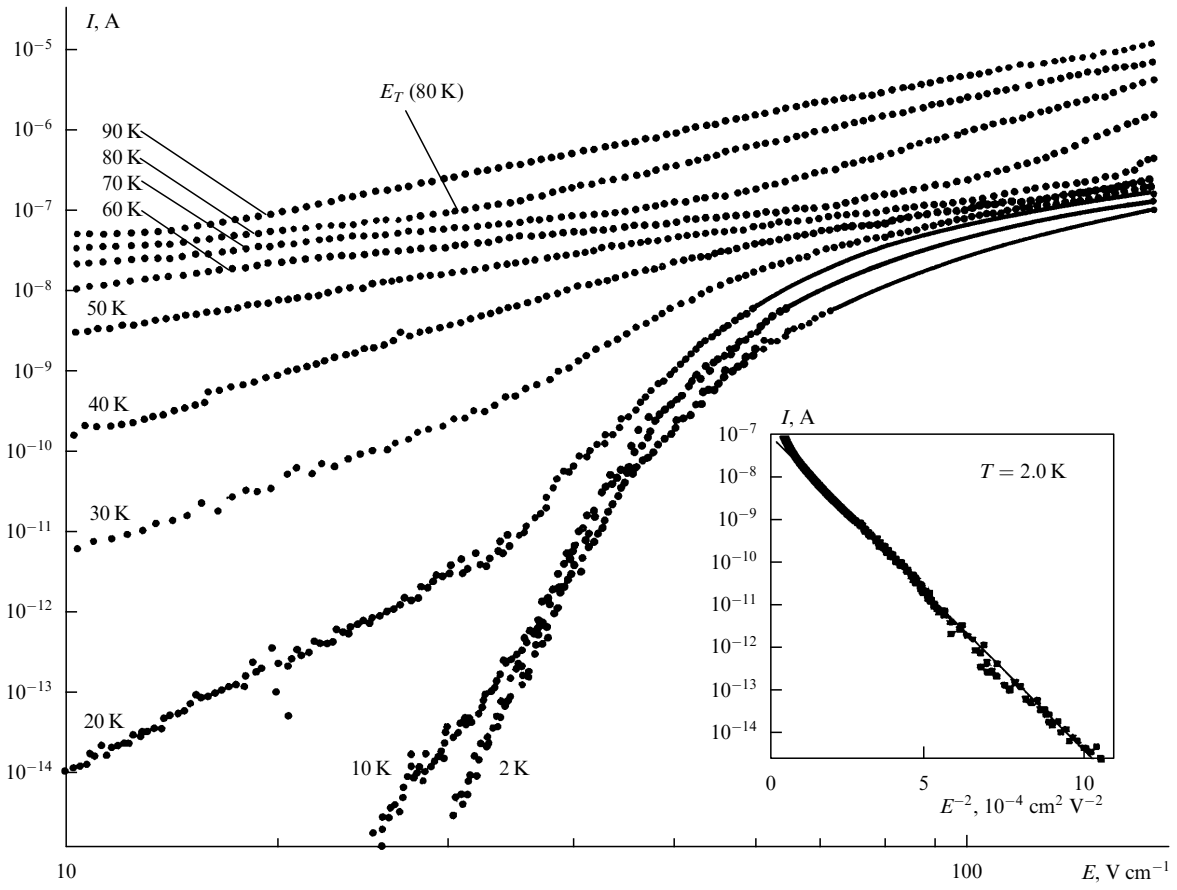

Figure 1. Temperature evolution of volt-ampere characteristics of a thin TaS_3 sample (cross-sectional area of 10^{-2} μm^2). The vertical arrow indicates the threshold field for the onset of CDW sliding at 80 K. Insert shows the variation of the nonlinear current with $1/E^2$ at $T = 2$ K. Data are from Ref. [18].

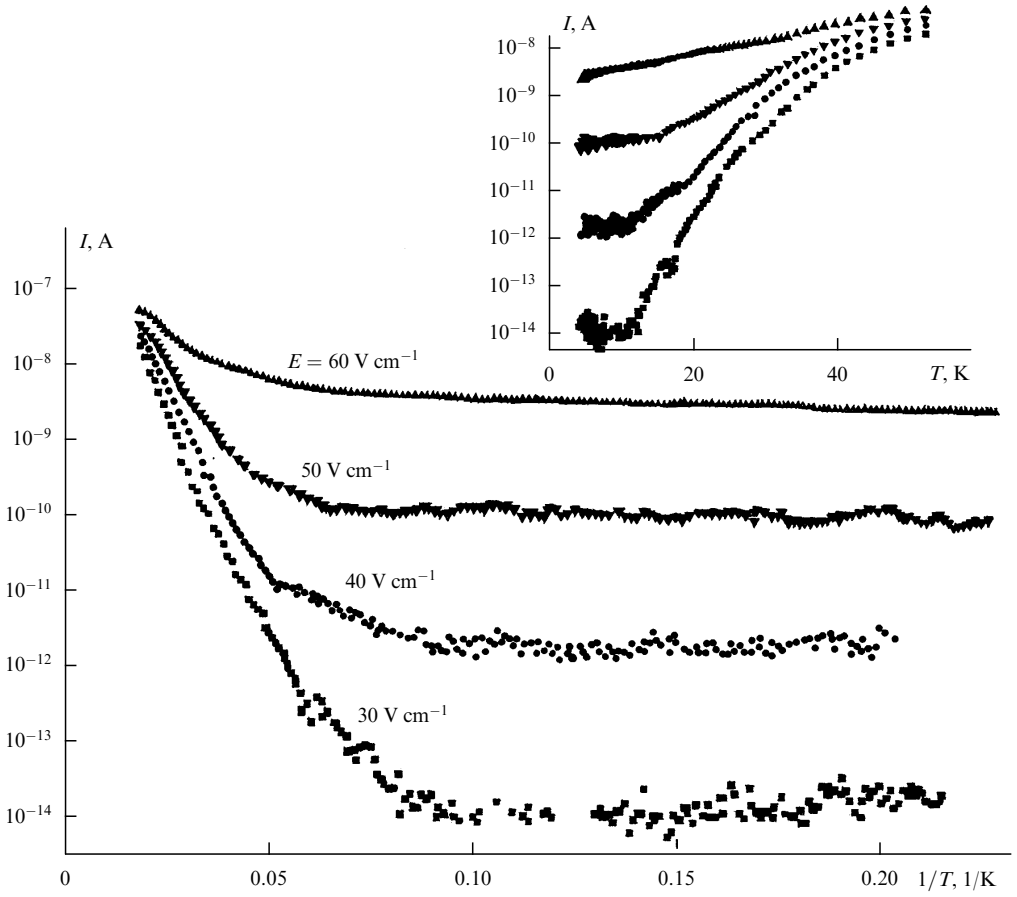

Figure 2. The nonlinear current versus the inverse temperature for the same TaS_3 sample as in Fig. 1. The numbers alongside the curves indicate the strength of the electric field. Insert shows the same data as a function of the temperature. Data are from Ref. [18].

point is that such motion involves the entire cross section of the sample, which can also be interpreted as the motion of domain walls blocking the sample cross section.

This behaviour of nonlinear conductivity in thin samples described above is different from that for TaS_3 samples of ordinary size. The decrease in the slope of $d \ln I / d(1/T)$ as the temperature is lowered below 20 K is well known for ordinary size samples. At the same time, the low-temperature conductivity of such samples displays different character. In particular, Ref. [20] reports an activated dependence of the nonlinear conductivity at $T < 20$ K, which suggests that $I(T) \to 0$ as $T \to 0$. At present there exists a model which leads to volt-ampere characteristics of Eqn (1); this is the phase slip process associated with the tunnel-assisted creation of a critical-radius dislocation loop [21]. A similar result was obtained by Maki [22]. Both models were proposed to explain the experimental data of Ref. [18].

4. Field effect

Recently, structures analogous to the transistor MIS structure have been manufactured with the conducting channel made of a quasi-one-dimensional conductor [23]. As in the conventional field transistor, application of a voltage to the gate of such a structure produces an electric field between the channel (thin crystal of a quasi-one-dimensional conductor) and the gate. The field penetrates the quasi-one-dimensional conductor and is screened over about 10 A. In the metal state (i.e. at a temperature above the Peierls transition temperature) the gate voltage response of such structures is relatively small (of order 1% for a sample with a cross section of 10^{-3} μm^2). It is associated with a change in the current carrier concentration due to the transverse electric field, and is close to the expected value [23]. Below the transition temperature, the screening of the transverse field also involves a charge density wave, which makes the behaviour of the system richer and much more complex as compared to regular field transistors. Figure 3 gives an idea of the variation of the nonlinear conductivity with the gate voltage, as well as of the size of the effect. The most intriguing result is that the gate voltage response of the CDW by far exceeds that of the quasiparticles. In particular, changing the gate voltage allows CDW motion to be switched on/off (see Fig. 3), whereas the linear conductivity remains essentially unchanged. A similar nonlinear conductivity behaviour is also disclosed in TaS_3 [23].

There is at present no comprehensive explanation of the observed effect. Theoretically, the effect of a field in quasi-one-dimensional conductors was treated by Matveenko and Brazovskiĭ [24] before the experimental work of [23]. They showed that the CDW participates in the screening of the transverse electric field because of the appearance of CDW dislocations. The fact of this participation is confirmed by measurements of the temperature-dependent linear response [23], which changes little when the CDW forms. At the same

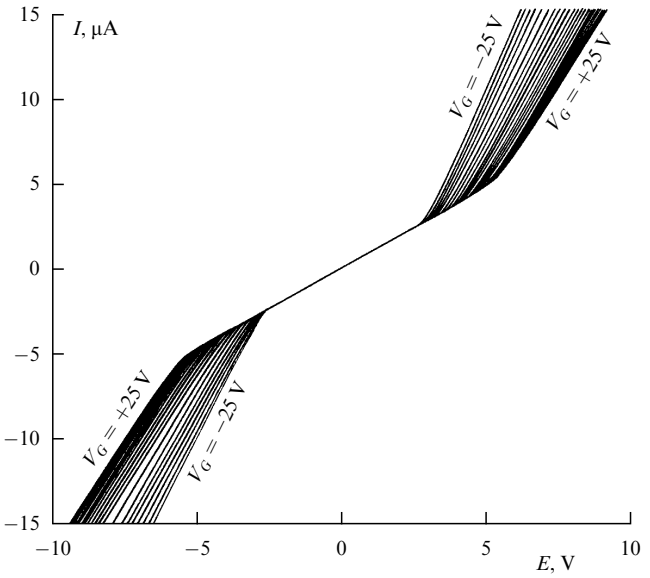

Figure 3. Volt-ampere characteristics of a $NbSe_3$ sample with cross section of 1.1×10^{-3} μm^2 at 30 K for the gate voltage variation in the range from −25 to 25 V by 2.5-V steps. Data are from Ref. [23].

time, a possible influence of the dislocations on CDW kinetics is not a critical factor, since the observed effect is odd in the gate field strength, whereas the dislocation concentration must be an even function of the gate voltage. The main contribution to the observed effect is presumably due to the modulation of the CDW order parameter with the change of an electron concentration in the screening region [23], although quantitative calculations are at present difficult because of the uncertainty in some of the parameters involved.

5. Conclusions

Thus, in addition to exhibiting ordinary one-electron conduction, CDW materials possess a conduction mechanism associated with collective degrees of freedom for the motion and deformation of the electron crystal, i.e. CDWs. These may be controlled by means of external fields: by influencing the one-particle conductivity mechanism, both the CDW-related conductivity and the electron and hole concentrations can be varied. While the properties of CDW conductors have been fairly well studied, many fundamental questions, notably the CDW behaviour at low temperatures, and the properties of solid-state structures with quasi-one-dimensional CDW conductors, remain to be answered.

References

1. Grüner G *Density Waves in Solids* (Reading: Addison-Wesley, 1994)
2. *Charge Density Waves in Solids* (Eds L Gor'kov, G Grüner) (Amsterdam: Elsevier Science, 1989)
3. Lee P A, Rice T M *Phys. Rev. B* **19** 3970 (1979)
4. Artemenko S N, Volkov A F *Zh. Eksp. Teor. Fiz.* **81** 1872 (1981) [*Sov. Phys. JETP* **54** 992 (1981)]; Chapter 9 in [2]
5. Takoshima T et al. *Solid State Commun.* **35** 911 (1980)
6. Higgs A W, in *Springer Lecture Notes in Physics* (Eds G Hutirai, J Solyom) **217** (1985) p. 422
7. Smontara A et al. *J. Phys. Condensed Matter* **4** 3273 (1992)
8. Yang Jie, Ong N P *Phys. Rev. B* **44** 1991 (1991)
9. Kriza G et al. *Solid State Commun.* **79** 811 (1991)
10. Nad F Ya, Monceau P *Solid State Commun.* **87** 13 (1993); *Synth. Metals* **70** 1255 (1995)
11. Volkov A F *Phys. Lett. A* **182** 433 (1993)
12. Larkin A, Brazovskiĭ S *Solid State Commun.* **93** 275 (1995)
13. Horovitz B, Krumhansl J A, Domany E *Phys. Rev. Lett.* **38** 778 (1977)
14. Brazovskiĭ S A, Matveenko S I *Zh. Eksp. Teor. Fiz.* **99** 887 (1991) [*Sov. Phys. JETP* **72** 492 (1991)]
15. Artemenko S N, Glyaisberg F *Pis'ma Zh. Eksp. Teor. Fiz.* **61** 762 (1995) [*JETP Lett.* **61** 779 (1995)]
16. Artemenko S N, Gleisberg F *Phys. Rev. Lett.* **75** 497 (1995)
17. Ioffe L B et al. *Pis'ma Zh. Eksp. Teor. Fiz.* **59** 65 (1994) [*JETP Lett.* **59** 65 (1994)]
18. Zaitsev-Zotov S V *Phys. Rev. Lett.* **71** 605 (1993); **72** 587 (1994)
19. Itkis M E, Nad F Ya, Monceau P *J. Phys. Condensed Matter* **2** 8327 (1990)
20. Duan Ji-Min *Phys. Rev. B* **48** 4860 (1993); *Phys. Rev. Lett.* **72** 586 (1994)
21. Adelman T L, Zaitsev-Zotov S V, Thorne R E *Phys. Rev. Lett.* **74** 5264 (1995)
22. Maki K *Phys. Lett. A* **202** 313 (1995)
23. Matveenko S, Brazovskii S *Synth. Metals* **55–57** 2696 (1993)

PACS numbers: **75.80.+q**

Giant magnetoresistance, spin-reorientation transitions, and macroscopic quantum phenomena in magnetic nanostructures

V V Dobrovitskiĭ, A K Zvezdin, A F Popkov

1. Introduction

Traditionally, the elaboration of magnetism in general and the study of new magnetic materials in particular have stimulated considerably the invention and development of new magnetic memory devices.

Recent technological advances have made it possible to fabricate ultrathin films with a practically perfect crystal structure and to design, on their base, fundamentally new magnetic materials: multilayered magnetic structures and superlattices. The discovery of the giant magnetoresistance effect in such systems has, first and foremost, spurred the development of superdense magnetic memory (planned as 10 Gbit/in.^{2} to 2010) [44]. New technologies based on electron-beam lithography [42] make it possible to produce magnetic 35 – 75-nm-diameter and 50 – 100-nm-period piles in a nonmagnetic matrix, securing a vertical record density of up to 65 Gbit/in.^{2}. However, the recent progress in the development of low-dimensional magnetic structures also permits their use in other applications, some of them being much closer to traditional semiconductor electronics applications. This is because semiconductor electronics is now approaching its limits, particularly in terms of dissipated power. In some cases, magnetic nanostructures (say, a spin transistor known for its lower dissipative power) enable many problems to be solved [45].

An alternative direction allowing to minimise dissipative power is the reversible quantum computer idea.

According to R Feynman, in such a computer, to each element of the Boolean algebra one can put in correspondence a Hamiltonian defined in the space of the states of a bistable system, the states compatible with appropriate information bits. Calculations are carried out using the quantum-mechanical evolution law as given by the Schrödinger equation

$$\psi(t) = \exp(-i\hat{H}t)\,\psi(0),$$

which is time reversible and information-conserving. The bistable states of elementary spins suit this idea best. In this case, the problem of the coupling of elementary states with the macroworld, i.e. the information input-output problem, is easier to handle.

A simple example of a realised Boolean operation in Feynman's approach is a particle of an easy-plane ferromagnet which starts to precess with a frequency $\omega_h = \gamma H$ as a magnetic field is turned on. One half-period of this precession realises the Boolean negation operation 'NOT', since the state of the particle changes to the opposite. If the precession field is created by stray fields from two neighbouring particles distant equally in opposite directions, then the fields on a particle either add or subtract depending on the particles's states, and during the half-period of precession in the resulting field, the controlled 'NOT' operation is realised. One can take a chain of spins to construct a logical automaton with a prescribed Boolean logic function. This requires a parallel time control of data input-output, for which purpose a chain-propagating magnetic-moment-flip wave, alias a magnetic soliton, can be used.

The bistable two-level system in a Feynman computer may be represented by a mesoscopic spin of a magneto-anisotropic particle with energy-degenerate equilibrium states. The ground state of such a particle is split owing to the macroscopic quantum coherence of the spins. Instead of the eigenfunctions of the ground and excited states, however, it is more convenient to deal with the coherent states of the magnetisation polarisation along two equivalent directions. The strong exponential dependence of the tunnelling frequency on the potential barrier height, $\Gamma = \exp \times \left[-U(H)/\hbar\Omega_0\right]$, suggests the use of Boolean elements employing the parametric decrease of the barrier height in the effective magnetisation field (dipole or exchange) exerted by the neighbouring particles. Owing to the exponential dependence of the tunnelling rate, the data output error probability in multi-input elements like the twice controllable 'NOT' is reduced as compared to the resonance elements discussed above.

Although our discussion so far has been primarily concerned with the potential applications of magnetic nanostructures, one further aspect of the subject is of no less interest: being as they are of mesoscopic size, such systems span the bridge between the macro- and micro-world and thus enable a study of problems related to the transition from the quantum mechanical to macroscopical description [43]. Such problems, being extremely attractive due to their fundamental significance, emphasise the importance of magnetic nanostructure studies.

2. Giant magnetoresistance and the spin-valve effect in multilayered structures

The giant magnetoresistance (GMR) effect [2, 3] is observed in many multilayered structures with magnetic layers separated by nonmagnetic metal layers about 10 – 20 A thick (Fe/Cr/Fe, Co/Cu/Co, Fe/Cu/Fe, NiFe/Cu/NiFe, etc.). The resistance is larger in antiferromagnetic configurations, i.e. when the magnetisation of neighbouring layers is antiferromagnetic, and is reduced by the action of a magnetic field which induces a transition to a ferromagnetic configuration. The size of the effect is defined as $\Delta R/R = (R_{\uparrow\downarrow} - R_{\uparrow\uparrow})/R_{\uparrow\uparrow}$, where $R_{\uparrow\downarrow}$ and $R_{\uparrow\uparrow}$ are the resistances in the antiferromagnetic and ferromagnetic configurations, respectively. In Co/Cu superlattices, $\Delta R/R$ reaches a value of 65% at room temperature in a magnetic field of order 10^4 Oe [4].

The physical basis for the effects we consider is the phenomenon of spin-dependent electron scattering. It is essential that the spin-flip mean free path of an electron in a multilayered structure much exceeds the thickness of each of the layers.

There are several theoretical approaches to the magnetoresistive effect. The essential details, however, can be accounted for by a simple phenomenological model which (i) assumes that, for antiferromagnetically oriented magnetisations in neighbouring layers, a fixed-spin electron has a different chemical potential in different magnetic layers, depending on whether the spin is parallel or antiparallel to the layer magnetisation vector, and (ii) includes the roughness of the magnetic barriers that emerge in the antiferromagnetic configuration. The magnetoresistance can be represented by [5]

$$\frac{\Delta R}{R} \approx \frac{4\Lambda_0}{3D}\,\frac{U}{E_F}\left(\ln\frac{2\Lambda_0}{D}\right)^{-1}, \qquad (1)$$

where Λ_0 is the electron mean free path in the ferromagnetic phase, D is the period of the structure, and U/E_F is the ratio of the exchange energy to the Fermi energy. By substituting the typical values of $\Lambda_0/D \approx 5$ and $U/E_F \approx 0.1$ into (1), we estimate $\Delta R/R \approx 0.3$.

Current GMR studies involve two geometries: longitudinal (CIP, current in the plane) and transverse (CPP, current perpendicular to the plane). Although the transverse effect is much larger, most of present studies are carried out in longitudinal geometry since CPP experiments are complicated by the fact that the total transverse resistance of the structure is very high [5]. This necessitates a search for other, contactless, methods for studying the transverse GMR. A possible answer [6] is that the kinetics of conduction electrons manifests itself not only in the low-frequency transport phenomena, but also in the optical properties of the structures, notably in the light reflection coefficient r. Thus, the conductivity difference between the ferromagnetic and antiferromagnetic orientations can be detected by the corresponding change Δr in the light reflection coefficient. A plot of $\Delta r/r$ against the incident frequency is given in Fig. 1. It should be noted here that although the magnitude of the effect is just a few percent, it is amenable to an experimental study. For comparison, the magnitude of the magnetooptical Kerr effect in multilayers is also a few percent.

3. Spin-reorientation transitions in multilayers

Phase diagrams determining the transformation of magnetic structures in a magnetic field are major characteristics of any magnetic system. Moreover, as mentioned above, the mutual orientation of magnetisation in different layers determines the magnitude of magnetoresistance. Thus, the study of orientation transitions and of the corresponding phase diagrams is one further important direction in the physics of multilayer structures.

We can take as our prototype the diagram of a three-layer structure. This structure is of great interest per se and used in many experiments as well as in practical applications (spin-valve effect [7], spin transistor [8], etc.). In particular, in the three-layer Gd/Pt/Co structure, an unusual phenomenon of 'negative coercivity' was detected [9], in which a system in a positive external magnetic field undergoes a transition to a

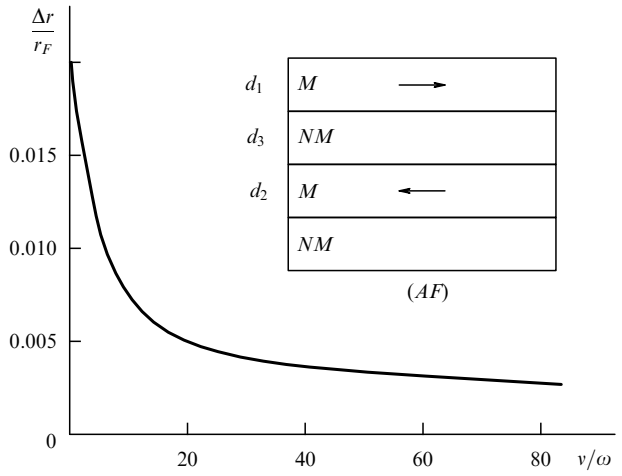

Figure 1. Fractional change of the reflection coefficient, $\Delta r/r_F$, versus light frequency: $\Delta r = r_F - r_{AF}$, where r_F (r_{AF}) is the reflection coefficient for ferromagnetically (antiferromagnetically) oriented magnetisations of neighbouring layers.

negative magnetisation. Here, unusual feature is that the system does not transit to the equilibrium minimum-energy state, but rather to a metastable one with a total magnetisation vector opposite to the external field strength. The same Ref. [9] suggests a qualitative understanding of this behaviour of a highly anisotropic three-layer structure. A more detailed theoretical study of the structure has revealed a number of new and important features crucial for the understanding of magnetisation processes in three-layer structures. The model employed was the structure of the type used in Ref. [9], i.e. an isotropic (magnetically soft) higher magnetised Gd layer is separated by a nonmagnetic (Pt) interlayer from a highly anisotropic (magnetically hard) and less magnetised Co layer (see Fig. 2). Thus, the free energy of the system divided by the structure thickness D can be put in the form

$$F = -\frac{d_1}{D}\, m_d H\cos\theta - \frac{d_1}{D}\, K_d\cos^2\theta - \frac{d_2}{D}\, M_f H_{\text{eff}} - \frac{d_2}{D}\, TS(M) + \frac{d_2}{D}\, aM_f^2 . \qquad (2)$$

Here H is the external magnetic field strength; m_d and d_1 are the magnetisation and thickness of the d-layer; M_f and d_2 are the same for the f-layer; $S(M)$ is the entropy of the f-subsystem; aM_f^2, the exchange energy; K_d, the magnetic anisotropy constant of the d-subsystem, including the bulk and interface contributions; θ, the angle between the external field and the d-layer magnetisation; H_{eff}, the effective magnetic field which acts on the f-ions and is given by

$$H_{\text{eff}} = (H^2 + \lambda^2 m_d^2 - 2\lambda m_d H\cos\theta)^{1/2} , \qquad (3)$$

here λ is the effective exchange constant determining the exchange field $H_{\text{ex}} = \lambda m_d$ exerted on the f-ions by the d-layer. Equation (2) takes care of the fact that $M_f \,||\, H_{\text{eff}}$ and the external field is directed along the easy magnetisation axis.

The phase diagrams for the strongly anisotropic ($H_a > \lambda m_d$) and weakly anisotropic ($H_a < \lambda m_d$) cases are given in Fig. 3. An interesting feature of the phase diagram for the latter case (Fig. 3a) is the line HG corresponding to the first-order phase transition from the magnetic to the angular structure. At such a transition, the magnetisation curve (corresponding to the motion along the KK' line of the diagram) must exhibit hystereses in the field range where the transition to the angular phase occurs. This is precisely the hystereses found in Ref. [9] (see insert in Fig. 3a) on Co(30 A)/Pt(5.2 A)/Gd(30 A) samples at 4.2 K in an external field of $H \approx 4$–7 Oe.

Conspicuous in the strongly anisotropic diagram (Fig. 3b) are the trajectory KK' and the corresponding hysteresis line. An interesting feature of this phase diagram is the presence of an angular phase in the region bounded by the HCG curves. This angular phase continues into the region above the $EHGF$

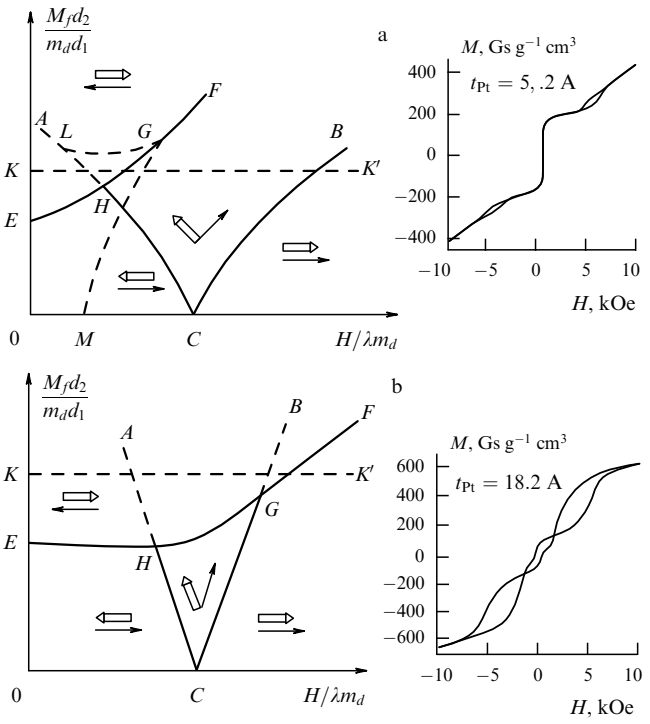

Figure 3. Phase diagrams of a three-layer magnetic structure: (a) $H_a < \lambda m_d$, (b) $H_a > \lambda m_d$, $H_a = 2K_d/m_d$. In Fig. 3a, HC, CB, and GF are the curves of the second-order phase transition; EGH, of the first-order transition; AH, GM, and GL are the stability loss curves for the corresponding phases. In Fig. 3b, EH, HG, and GF are the curves of the first-order phase transition; HC and CG, of the second-order transition; AH and GB, the stability loss curves for the metastable angular phase. Curves KK' in both diagrams correspond to the typical hysteretic curves shown in the inserts (experimental curves in the inserts are taken from Ref. [9]).

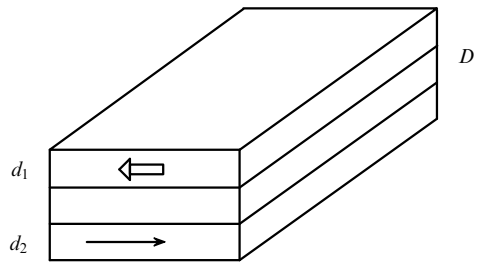

Figure 2. Three-layer structure. Top: anisotropic layer of thickness d_1 (Co); bottom: isotropic layer of thickness d_2 (Gd). In the middle: nonmagnetic layer (Pt). The overall structure thickness is D.

curve, but is metastable there. On passing through this phase, the magnetisation of the strongly anisotropic Co subsystem deviates slightly from the easy magnetisation axis, and the isotropic (Gd) subsystem undergoes a 180° reorientation. The same process takes place above the *EHGF* curve, thus securing a continuous uniform magnetisation reversal of the three-layer structure. The hysteretic curve shown in the insert in Fig. 3b is of particular interest since it demonstrates the negative coercivity effect mentioned above. The mechanism of uniform magnetisation reversal thus found in the three-layer structure seems to be of special importance for spin-valve elements. The uniformity of the process holds a promise of high switching rates being achieved in such elements. There is a definite and deep analogy between this magnetisation reversal mechanism and Jahn–Teller's cooperative magnetic effect [10].

The basic peculiarities of the phase diagrams in Fig. 3 also occur in the case of anisotropic magnetic superlattices with an antiferromagnetic exchange interaction between neighbouring layers [11, 12]. A characteristic feature of the phase diagrams of magnetic superlattices (Figs 4, 5) is the specific surface phases (for example, the regions bounded by the *EPLG* and *PLA* curves in Fig. 4).

4. Quantum fluctuations

In this section we shall discuss other interesting effects, occurring not only in quasi-two-dimensional ultrathin magnetic films but also in quasi-one-dimensional ultrathin wires and 'zero-dimensional' small magnetic particles. These are macroscopic quantum tunnelling (MQT) and macroscopic quantum coherence (MQC). The term 'macroscopic quantum tunnelling' usually implies the decay of a metastable level into a continuum via a coherent quantum tunnelling of a macroscopic, or at least mesoscopic number of strongly coupled quantum entities (in our case, spins). A closely related phenomenon is MQC in a two-well potential. In this case each degenerate level in either well splits in two ones due to the interwell tunnelling of a macro- or mesoscopic number of quantum entities (Fig. 6).

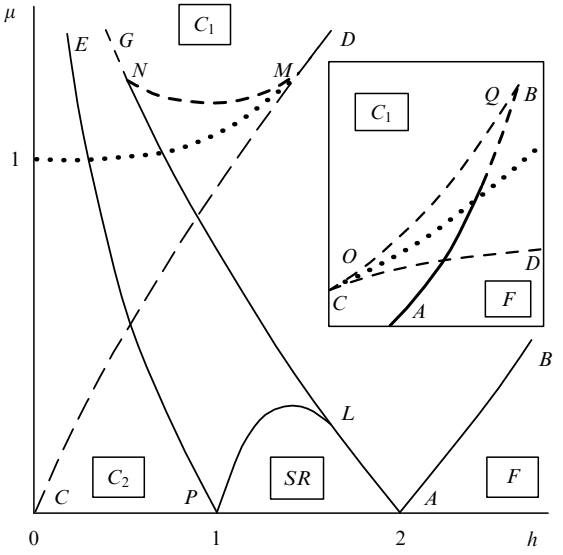

Figure 4. Phase diagrams for anisotropic superlattices with an antiferromagnetic exchange interaction between neighbouring layers. The external field is along the easy axis. To the right of the curve *AB* lies the ferromagnetic phase *F*. The C_1 and C_2 phases are antiferromagnetic. In the former, the magnetisation of *f*-layers is along the external field, and that of *d*-layers, against; in the latter, on the contrary, *f*-layers are magnetised against the field, and *d*-layers, along. *PLA* curves bound the surface-reoriented phase *SR*, with a ferromagnetic structure on the surface and an antiferromagnetic one in the bulk. *EPLG* curves bound another surface phase, with an angular configuration localised near the surface.

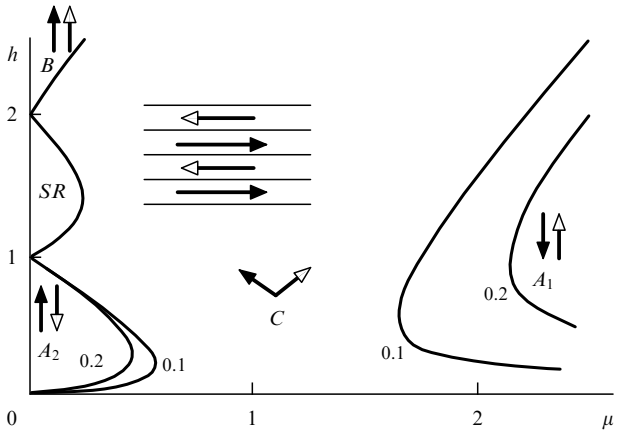

Figure. 5. Phase diagrams for anisotropic superlattices with an antiferromagnetic exchange between neighbouring layers. The external field is normal to the easy axis. Regions of existence of each phase are calculated for two dimensionless anisotropy energies *K*: $K = 0.1$ and $K = 0.2$.

The possibility of detecting MQT magnetisation experimentally was first suggested in Ref. [13]. To date, many experiments have been performed, whose results are considered as experimental evidence for MQC and (mostly) MQT effects [14]. Among the materials studied are small ferromagnetic and antiferromagnetic particles, the ultrathin films and multilayers including structures like domain wall (DW) junctions [15], and even bulk samples of ordered [16] and disordered [17] magnetic materials.

Current MQT (as well as MQC) studies employ the method of trajectory integration in imaginary time (i.e. with the replacement $t \to i\tau$), which allows a rapid and elegant change from the classical to the quantum description. Such an approach to the problem of the metastable state decay was developed in Refs [18, 19]. The decay rate is written in the form

$$\Gamma = \exp(-B), \qquad B = \frac{S_{\text{inst}}}{\hbar}, \tag{4}$$

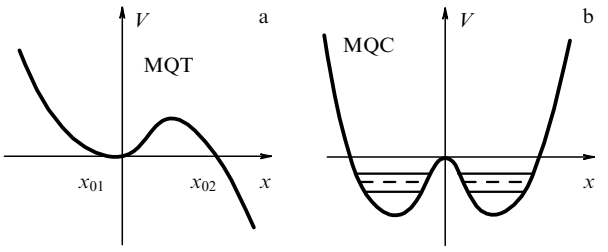

Figure 6. Characteristic shapes of MQT and MQC potentials. (a) A system initially localised within a local minimum (near x_{01}) tunnels to the right, beyond x_{02}. (b) Levels degenerate in the absence of tunnelling are shown by dashes. Tunnelling lifts the degeneracy, and each level splits in two levels (shown by solid lines).

where S_{inst} is the classical action as calculated on the so-called instanton trajectory which starts at point x_{01} (Fig. 6) for $\tau \to -\infty$, passes point x_{02} at $\tau = 0$, and terminates at x_{01} as $\tau \to +\infty$. For problems of the type we consider, this approach is the simplest and sometimes the only one possible.

The process of MQT magnetisation has been studied theoretically in Ref. [20], however, the corresponding relaxation rate and the temperature of the crossover (from the thermally activated jumps over the barrier to quantum tunnelling through it) turned out underestimated. The next major step was taken in Ref. [21], which examined tunnelling through the anisotropy-induced barrier in a small antiferromagnetic particle. In this case, the crossover temperature turned out to be fairly high, on the order of a few kelvins. At present, however, it is magnetic solitons, i.e. domain walls, vortices, vertical Bloch lines, etc., which are considered most suitable for experimental MQT studies. The reason is that, owing to their solitonic nature, these objects are to a large extent decoupled from their dissipative environment, i.e. from the elementary excitations of the magnetic medium — magnons (the interaction with them comes only in a second-order perturbation analysis, see Ref. [14]). In addition to practical and experimental applications (fundamental limitations on the data record density on magnetic storage devices, a detailed study of MQT and related research directed at the development of quantum computers), theoretical investigations in this area are of interest in itself as elucidating the quantum behaviour of magnetic solitons. The early work on MQT domain walls (DW) in various materials was done by Egami [22] and later by Chudnovski et al. [23]. These studies, however, were limited to the linear regime of DW dynamics. The nonlinear regime, namely the relation between MQT characteristics and the nonlinear dynamical properties of a DW itself, was examined in Ref. [24].

The physical model employed involves DW tunnelling through an external pinning potential in a weakly ferromagnetic (WFM) (e.g., orthoferrite) material. Use is also made of a well-known phenomenological model, in which the movement of a DW through the pinning potential proceeds by succession of fluctuative movements of small individual portions of the wall, thermally activated at high temperatures and quantum at low temperatures [17]. Such an approach thus naturally focuses on the small portion of the DW directly involved in tunnelling. Clearly, this particular portion lags behind the motion of all the other portions, not fixed by the defect, so the wall turns out to be bent in the defect region. However, if the radius of the curvature much exceeds the DW thickness, the corresponding energy is merely a correction, and to describe the dynamics of the system it suffices to consider the DW as plane (the details of this approach have been discussed in the review [14]).

Thus, the domain wall is considered one-dimensional, and its position can be characterised by a single coordinate x_0, the position of its centre. For a two-sublattice model of $YFeO_3$-type WFM material, the Lagrange function, or more precisely the Lagrangian density per DW unit area, may be obtained (for real time t) using the perturbation theory for solitons [25, 26] to give

$$L = -mc^2\sqrt{1 - \frac{v_0^2}{c^2}} - U(x_0), \tag{5}$$

where x_0 is the position of the DW centre; $v_0 = \dot{x}_0$ is its velocity; $mc^2 = 2\sqrt{A(K_{ac} + \chi_\perp H^2)}$; K_{ac} is the anisotropy constant for the crystallographic plane ac, in which the antiferromagnetic vector $\mathbf{l}$ rotates; A is the nonuniform exchange constant; $\chi_\perp$ is the transverse susceptibility of the WFM material; and, finally, $U(x_0) = -\int 2M_z^0 H(x_0)\,\mathrm{d}x_0$ is the potential, where $H(x_0)$ is the total external magnetic field acting on the wall, which includes both the external drive field and the effective field created by the defect.

To proceed further, however, the standard use of imaginary-time path integrals is strictly invalid, since the standard form of a path integral is only good for Lagrangians quadratic in the velocity [27]. Our starting point should therefore be the Hamiltonian formulation of the functional integral for the transition amplitude:

$$\rho(x,y) = \int_{(q=x)}^{(q=y)} Dq \int_{(-\infty)}^{(+\infty)} \frac{Dp}{2\pi\hbar} \exp\left\{\frac{1}{\hbar}\int_0^T \mathrm{d}\tau\left[\mathrm{i}p\dot{q} - H(p,q)\right]\right\}, \tag{6}$$

where the variables p and q are canonically conjugate, and $H(p,q)$ is the Hamiltonian density per unit area. However, it can be shown [24] that in this case a WKB-approximated path integral can also be bring to the standard Wiener-normalised form. As before,

$$\Gamma = \exp(-B), \qquad \frac{B}{A_w} = \frac{S_{\text{inst}}}{\hbar}, \tag{7}$$

but the pre-exponential factor is now different (cf. [19]):

$$C = \sqrt{\frac{mv}{2\pi\hbar}}\left|\frac{\det'\left[-\partial_\tau\left\{(1/\bar{u}^2)\,\partial_\tau\right\} + (v_{\text{inst}})^2/m\right]}{\det\left[-m\partial_\tau^2 + \omega^2\right]}\right|^{-1/2}, \tag{8}$$

where

$$\omega^2 = \frac{1}{m}\left.\frac{\partial^2 U(x)}{\partial x^2}\right|_{x\equiv x_{01}}, \qquad (v_{\text{inst}})^2 = \left.\frac{\partial^2 U(x)}{\partial x^2}\right|_{x=x_{\text{inst}}}. \tag{9}$$

The quadrature for $x_{\text{inst}}(\tau)$ with an arbitrary potential U takes the form

$$\int_{x_{02}}^{x_{\text{inst}}} \frac{\mathrm{d}x}{\pm c\sqrt{(mc^2/\tilde{U})^2 - 1}} = \tau, \tag{10}$$

the choice of the sign depending on the direction of the motion. Similarly, the expression for S_{inst} is

$$S_{\text{inst}} = 2\int_{x_{02}}^{x_{01}} \sqrt{2mU(x) - \frac{\left[U(x)\right]^2}{c^2}}\;\mathrm{d}x. \tag{11}$$

It should be noted here that the results (10) and (11) are meaningful only if

$$\max_{x\in[x_{02},\,x_{01}]} U(x) < mc^2,$$

otherwise an instanton solution does not exist and the WKB tunnelling rate vanishes. In reality, of course, the DW will be able to tunnel in this case also, but at a rate of the next order in $\hbar$, meaning that the tunnelling will be to a large extent suppressed.

DW tunnelling experiments on terbium orthoferrite $TbFeO_3$ were carried out by the Tejada group [16]. Comparison with experiment (which we omit for the lack of space, see the original work [24]) yields reasonable and well consistent values for various tunnelling characteristics.

Mention should also be made of a successful effort now underway to study domain wall MQT in a controllable way using nanostructures expressly designed and grown for the purpose, namely DW junctions [15] and quasi-one-dimensional wires [28] mentioned above.

The study we have outlined was mainly concerned with the dynamical properties of the soliton as an essentially nonlinear entity. The soliton also has nontrivial topological characteristics, however, one of these being the topological charge. The problem of topological charge changes is a long-recognised one; in particular, at the microlevel such phenomena play an important role in determining the existence of a gap in the elementary excitation spectrum of a two-dimensional antiferromagnetic [29]. At the macroscopic level, Ref. [30] presents a study of the tunnelling-induced change of the topological charge of a vortex structure in a two-dimensional antiferromagnetic.

An analogous effect in an ultrathin ferromagnetic film was studied in Ref. [31]. Within domain walls in uniaxial, perpendicular anisotropy ferromagnets, another vortex structures — the vertical Bloch lines (VBL) — exist. In a certain approximation, such a structure may be described by Slonczewski's equations in terms of two variables: the position of the DW centre q , and the azimuthal angle within the wall, ψ. The topological charge of a VBL is specified by the boundary conditions; we shall assume that initially (for $t \to -\infty$) $\psi(x \to -\infty) = 0$, $\psi(x \to +\infty) = -\pi$. This configuration has the same energy as that with an opposite charge: $\psi(x \to -\infty) = 0$, $\psi(x \to +\infty) = \pi$, so that this degeneracy can be lifted by tunnelling. The transition matrix element, in the WKB approximation, is readily calculated by the functional integration method. The instanton in this case will be the field configuration $\psi(x, t)$ shown in Fig. 7, with a singular point $x = 0$, $t = 0$. The action for the instanton configuration is of the form

$$S_{\text{inst}} \approx \frac{16Ad}{\sqrt{2\pi\gamma^2 K}} . \tag{12}$$

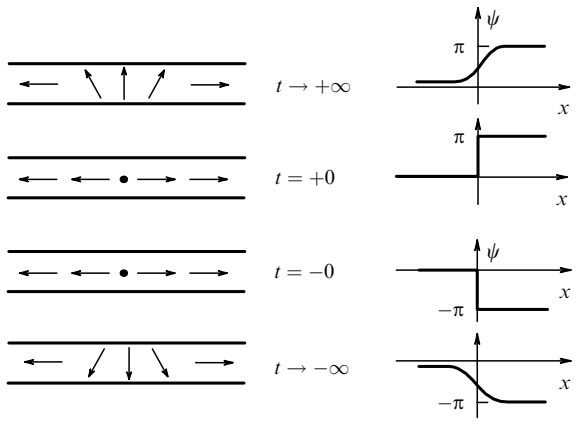

Figure 7. Instanton field configuration $\psi(x, t)$ corresponding to the tunnelling-induced change of the VBL topological charge. To the left: distribution of magnetisation at various instants of imaginary time; to the right: the corresponding $\psi(x, t)$ plots. The instants $t \to \pm\infty$ correspond to static VBLs with topological charge of opposite sign. At point $x = 0$, $t = 0$, the function $\psi(x, t)$ displays a discontinuity, with the energy (potential barrier height) diverging as $1/\sqrt{t}$.

An interesting and extraordinary feature of the problem is that in the continuum limit ($a/\Delta \to 0$, a is the lattice constant, Δ is the DW width) the height of the potential barrier diverges at the singular point ($x = 0$, $t = 0$), although the instanton action (and hence the tunnelling probability) remains finite; thus, the concept of the crossover temperature becomes meaningless.

The relationship between tunnelling and topology, however, is not limited to the tunnelling-assisted change of the topological charge. For spin systems, the topology of spin space is of great importance, determining the instanton interference effect if there exist alternative subbarrier tunnelling trajectories. This effect renders the magnetic particle ground state dependent on the parity of the number of elementary spins comprising the total spin [32, 33]. In an antiferromagnet, which always has an even number of elementary spins, the effect of Kramers freezing of the MQT in zero magnetic field is absent. However, when a magnetic field is turned on, the field dependence of the topological term in the action (known as the Berry phase) may give rise to a phase incursion in the tunnelling amplitudes, its value depending on the sign of the topological charge. This will then lead to a periodic freezing of macroscopic quantum phenomena and to field oscillations in the spin tunnelling rate [34, 35], i.e. a magnetic analogue of the Aharonov–Bohm effect. In the collinear antiferromagnetic phase, when the magnetic field is parallel to the equilibrium direction of the Néel vector and does not exceed the spin-flop value $H_{s-\text{flop}}$, no quantum interference occurs because the field contribution to the action topological term is zero. As the magnetic field is increased, the tunnelling probability rises exponentially because the energy barrier lowers as the critical spin-flop field is approached. Very close to the transition to the angular phase, however, the tunnelling rate drops sharply, turning to zero together with the resonance frequency at the very transition point. The dependence of the Néel vector tunnelling rate on magnetic parameters in a biaxial particle then has a usual form (4) with

$$S_{\text{inst}} = 2V\gamma^{-1}\left[K\chi_{\perp}\left(1 - \frac{H^2}{H_{s-\text{flop}}^2}\right)\right]^{1/2}, \quad C = 8\hbar\omega\left(\frac{S_{\text{inst}}}{2\pi\hbar}\right)^{1/2},$$

where V is the particle volume; γ, the gyromagnetic ratio; $\chi_{\perp}$, the magnetic susceptibility; K is the anisotropy constant, and $\omega = \gamma H_{s-\text{flop}}(1 - H^2/H_{s-\text{flop}}^2)^{1/2}$, the resonance frequency.

In the angular phase, because of the quantum interference of the instantons, the tunnelling rate oscillates in the magnetic field as follows:

$$\Gamma = C\exp\left(-\frac{S_{\text{inst}}}{\hbar}\right)\left|\cos\frac{2\pi H}{H_{s-\text{flop}}}\right|. \tag{13}$$

The envelope of the oscillations increases exponentially until the spin-flop field is reached, where it drops sharply to zero.

Among antiferromagnets with a narrow magnetic resonance line, the yttrium orthoferrite (a weak ferromagnet of orthorhombic symmetry) is of special interest. The presence of spontaneous magnetisation and low dissipation make it promising for resonance MQC experiments. Figure 8 shows the predicted [36] particle-size dependence of the antiferromagnetism-vector tunnelling rate in this material. The field-related features of macroscopic quantum phenomena in this material are closely related to the orientation dependence of

the equilibrium states of its magnetic system in the external magnetic field. Thus, when the field is applied along the *b* crystallographic axis, yttrium orthoferrite behaves like pure antiferromagnet with the angular phase. In this case, the interference of instanton amplitudes occurs, leading to oscillations in tunnelling rate as the magnetic field strength increases. The period of the oscillations is given by the exchange field divided by the number of elementary spins. The magnetic field dependence of the envelope of the MQT oscillations is illustrated in Fig. 9. If the magnetic field is parallel to the *a* axis of the atomic lattice, then there is no field-related topological addition to the tunnelling amplitude phase, and the tunnelling rate increases monotonically up to the magnetisation U-turn, and then drops sharply as shown in Fig. 10.

An interesting quantum interference phenomenon may arise in a weakly ferromagnetic particle when the magnetic field is directed against the magnetisation vector and along the crystal *c* axis, and the particle is in a metastable state in the magnetic hysteresis region. The tunnelling then proceeds in two stages: the subbarrier motion to the turning point, at

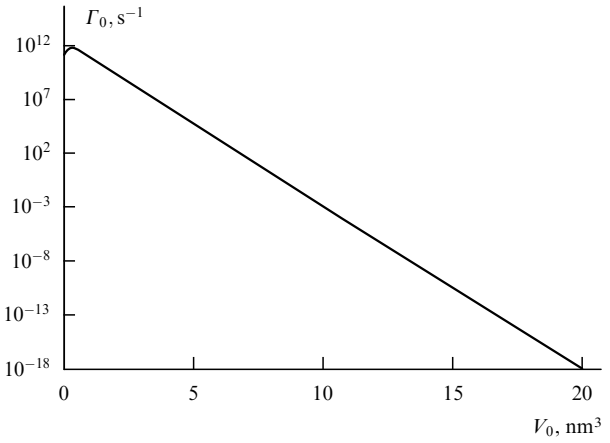

Figure 8. Tunnelling rate versus particle volume for $YFeO_3$.

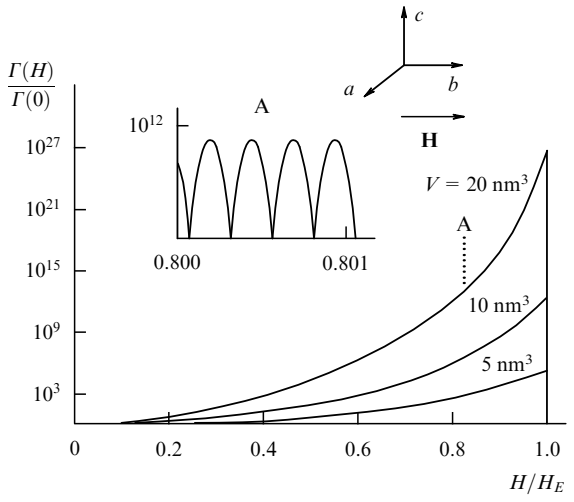

Figure 9. Dependence of the envelope of tunnelling rate on the external field strength along the *b* axis, for three values of the $YFeO_3$ volume. Insert: tunnelling rate oscillations due to the quantum instanton interference.

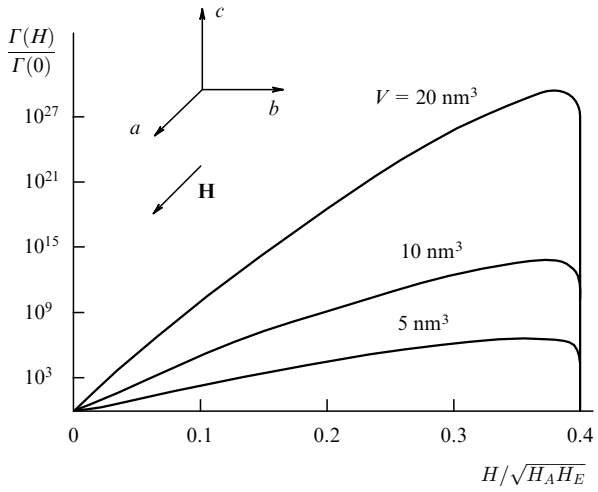

Figure 10. Dependence of the tunnelling rate on the external field applied along the *a* axis for three values of the $YFeO_3$ volume.

which the particle comes to the boundary of the tunnelling region, and the transition to a resonance level within a deeper potential well. In the absence of dissipation, coherent states at the turning points may transform in one another due to the coherent spin rotation at the resonance level. The resulting phase incursion in the probability amplitude is magnetic field dependent. Analysis shows that the interference arising between the tunnelling amplitudes may lead to a complete freezing of the metastable phase decay within the magnetic hysteresis region at a finite magnetic field, provided the sublattice spin is half-integer. However, the subtle interference effects we have considered may be easily destroyed by fluctuations in tunnelling amplitude phases, due to the interaction of the magnetic order parameter with its environment (elastic atomic-lattice deformations, spin waves, magnetic nuclei, and weakly coupled spins). These questions are discussed partly in Refs [37 – 39]. But their complete elucidation requires further investigation. Thus, analysis has shown that an MQC state persists up to very strong fields in an antiferromagnetic particle. Furthermore, the energy splitting concerned with MQT increases to very large values comparable to the frequency of a magnetic resonance near the orientation-phase transition lines. The large splitting at low temperatures, when the phonon heat capacity is exponentially small, must produce a marked jump-like contribution to the heat capacity of the particle at a certain temperature determined by the energy splitting. Estimates show that close to the orientation transition, the characteristic temperature is tens of mK. Thus, there is a possibility of an independent experimental verification of the MQC effect seen in antiferromagnetic hexaferrite particles [40].

In all of the studies cited, the starting point was the assumption that the modulus of the magnetisation vector conserves: $|\mathbf{M}| = \text{const}$. This condition is fulfilled only for weakly anisotropic materials, with relativistic effects much smaller than that of the exchange interaction. However, of the macroscopic quantum objects that have so far been studied, many are strongly anisotropic magnetic materials.

The strongly anisotropic limit — the Ising case — was considered in Ref. [41]: a small particle of a material in which the ground state of magnetic ions provides two closely lying

singlets of energy Δ apart, separated from the other excited levels by a gap much wider than Δ. Although there is no continuous magnetisation trajectory, the tunnelling probability is nonzero because of the inclusion of the quadrupole moment of the Ising ion. In this case, the argument B of the exponential in function (4), known as the Gamov constant, is

$$B = N\left(\ln\frac{1+\sigma_0}{1-\sigma_0} - 2\sigma_0\right), \tag{14}$$

where N is the total number of spins in the particle, and $\sigma_0 = [1-(\Delta/4\lambda)^2]^{1/2}$. It turns out that the corresponding crossover temperatures may be sufficiently large for the phenomenon to be experimentally detected: for $LiTbF_4$ this is 0.49 K, and for $Tb(OH)_3$, 0.81 K.

In recent years new and interesting objects, magnetic clusters, have received much attention. An example is Mn_{12} (Fig. 11). The cluster contains eight Mn^{3+} ions (of spin 3/2) antiferromagnetically coupled to four remaining Mn^{4+} ions (spin 2). The ground state of the cluster is $S = 10$. The system has a strong 'easy-axis' anisotropy, the higher order anisotropies being rather small. Nevertheless, such clusters exhibit a saturation of the magnetic relaxation rate at low temperatures [42] (characteristic of MQT), although it is known that in purely uniaxial particles tunnelling is completely frozen (the projection of the angular moment conserves). Although the situation is far from clear at present, the influence of dissipative environment may be one of the possible solutions to the paradox.

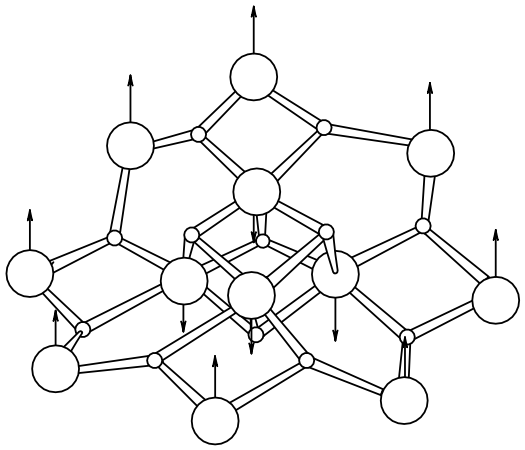

Figure 11. Cluster Mn_{12}. Eight Mn^{3+} ions (spin 3/2) are antiferromagnetically coupled to four Mn^{4+} ions (spin 2). The resulting ground state is one with a spin $S = 10$.

5. Conclusions

We have considered a wide spectrum of interesting and unusual phenomena occurring in low-dimensional magnetic structures such as ultrathin films, multilayer systems and superlattices, quasi-one-dimensional nanowires, and 'zero-dimensional' small particles. The effects considered appear to be of much interest both from the fundamental point of view and for practical applications including components for the further development of micro- and nanomagnetoelectronics.

References

1. Krauss P R, Fisher P E, Chon S Y *J. Vac. Sci. Technol. B* **12** 3639 (1944)
2. Baibich M N et al. *Phys. Rev. Lett.* **61** 2472 (1988)
3. Binasch G et al. *Phys. Rev. B* **39** 4828 (1989)
4. Parkin S S P, Li Z G, Smith D J *Appl. Phys. Lett.* **58** 2710 (1991)
5. Zvezdin A K, Utochkin S N *Pis'ma Zh. Eksp. Teor. Fiz.* **57** 418 (1993) [*JETP Lett.* **57** 433 (1993)]
6. Atkinson R et al. *J. Magn. Magn. Mater.* (1996) (in press)
7. Slonczewski J C *Phys. Rev. B* **39** 6995 (1989)
8. Johnson M *Science* **260** 320 (1993)
9. Takanashi K, Kurokawa K, Fujimori H *Appl. Phys. Lett.* **63** 1585 (1993)
10. Zvezdin A K, Matveev V M, Mukhin A A, Popov A I *Redkozemel'nye Iony v Magnitouporyadochennykh Kristallakh* (Rare Earth Ions in Magnetically Ordered Crystals) (Moscow:Nauka, 1985)
11. Utochkin SN, Zvezdin AK *J.Magn.Magn.Mater.***140-144** 787(1995)
12. Atkinson R et al. *J. Appl. Phys.* **75** 1 (1994)
13. Bean C P, Livington J D *J. Appl. Phys.* **30** 120S (1959)
14. Stamp P C E, Chudnovski E M, Barbara B *Int. J. Mod. Phys. B* **6** (9) 1355 (1992)
15. Gunther L, Barbara B *Phys. Rev. B* **49** 3926 (1994)
16. Zhang X X et al. *J. Magn. Magn. Mater.* **137** L235 (1994)
17. Uehara M, Barbara B *J. Physique* **47** 235 (1986)
18. Langer J S *Ann. Phys.* (New York) **41** 108 (1967)
19. Callan C G (Jr), Coleman S *Phys. Rev. D* **16** 1762 (1977)
20. Chudnovsky E U, Gunther L *Phys. Rev. Lett.* **60** 661 (1988)
21. Barbara B, Chudnovsky E U *Phys. Lett. A* **141** 205 (1990)
22. Egami T *Phys. Status Solidi* (*b*) **57** 211 (1973)
23. Chudnovsky E U, Iglesias O, Stamp P C E *Phys. Rev. B* **46** 5392 (1992)
24. Dobrovitskiĭ V V, Zvezdin A K *Zh. Eksp. Teor. Fiz.* **109** 1420 (1996) [*Sov. Phys. JETP* **82** 766 (1996)]
25. McLaughlin D, Scott A *Multisoliton Perturbation Theory* in: *Solitons in Action* (Eds K Lonngren, A Scott) (New York: Academic Press, 1978)
26. Zvezdin A K, Mukhin A A *Zh. Eksp. Teor. Fiz.* **102** 577 (1992) [*Sov. Phys. JETP* **75** 306 (1992)]
27. Slavnov A, Faddeev L *Vvedenie v Kvantovuyu Teoriyu Kalibrovochnykh Polei* (Introduction to the Quantum Theory of Gauge Fields) (Moscow: Nauka, 1971)
28. Kimin Hong, Giordano N *Phys. Rev. B* **51** 9855 (1995)
29. Haldane F D M *Phys. Rev. Lett.* **61** 1029 (1988)
30. Galkina E G, Ivanov B A *Pis'ma Zh. Eksp. Teor. Fiz.* **61** 495 (1995) [*JETP Lett.* **61** 511 (1995)]
31. Dobrovitskiĭ V V, Zvezdin A K *J. Magn. Magn. Mater.* (1996)
32. Loss D, Di Vincenzo D P, Grinstein G *Phys. Rev. Lett.* **69** 3232 (1992)
33. Von Delft J, Henley C L *Phys. Rev. Lett.* **69** 3236 (1992)
34. Duan Ji-M, Garg A *Physica B* **194–196** 323 (1994)
35. Galyshev V Yu, Popkov A F *Europhys. Lett.* **29** 327 (1995)
36. Galyshev V Yu, Popkov A F *Zh. Eksp. Teor. Fiz.* **108** 1755 (1995) [*Sov. Phys. JETP* **81** 962 (1995)]
37. Garg A *Phys. Rev. Lett.* **70** 1541 (1993)
38. Stamp P C E *Physica B* **197** 133 (1994)
39. Prokof'ev N V, Stamp P C E *J. Phys. CM* **5** L667 (1994)
40. Awschalom D D *Phys. Rev. Lett.* **68** 3092 (1992)
41. Zvezdin A K, Popkov A F *Pis'ma Zh. Eksp. Teor. Fiz.* **57** 548 (1993) [*JETP Lett.* **57** 562 (1993)]
42. Barbara B et al. *J. Magn. Magn. Mater.* **140–144** 1825 (1995)
43. Kadomtsev B B *Usp. Fiz. Nauk* **164** 449 (1994) [*Phys. Usp.* **164** 425 (1994)]
44. Simonds J L *Phys. Today* **48** 26 (1995)
45. Prinz G A *Phys. Today* **48** 58 (1995)

PACS numbers: 72.15.Rn, 73.20.Dx, 78.50.Ge

Controlled modulation of the binding energy of impurity states in a quantum-well system

V I Belyavskiĭ, Yu V Kopaev, N V Kornyakov

1. Impurity atoms and point defects in semiconductors not only act as scattering centres for current carriers, but, more important for practical applications, they serve as dopants, thus playing a constructive role as suppliers of free electrons or holes. The ionisation energy of impurity atoms in this case is an important parameter determining the concentration of free charge carriers and its temperature dependence. Controlling this parameter enables a very wide carrier concentration range to be covered due to the fact that the distribution function depends exponentially on the energy near the Fermi level.

In bulk semiconductors, the possibility of influencing the binding energy of an electron in an impurity atom (by an external electric field, for example) is extremely limited (to be specific, and unless otherwise stated, we consider impurities to be donor-type when speaking of electrons in what follows). This is due, in particular, to the fact that the electric field perturbs only slightly the continuum states, from which the localised state is formed. A different situation exists in semiconducting heterostructures (HS) formed on the base of composite semiconductors. Since the motion of electrons in quantum wells is restricted to layer planes, application of a relatively weak external electric field perpendicular to the layers may redislocate the electron wave function from one quantum well to another [1]. This causes an inversion of the lower dimensional quantisation subbands and, as a consequence, the localised state, which is formed primarily from the lowest subband, changes its binding energy and the shape of its wave function [2].

The strength of the external electric field necessary to redislocate the wave functions and to change the binding energy of an impurity state, depends essentially on the heterostructure parameters (barrier height, quantum-well width, etc). What is of fundamental importance here is the optimisation of these parameters to have the electron wave functions in the quantum-well system redislocated as much as possible at minimum electric field strengths. This can be achieved by choosing the quantum-well parameters such that without a field the extrema of the dimensional quantisation bands be close to one another, thus supplying the system with a necessary sensitivity to external influences. At the same time, due to the restricted nature of electron motion across the layers, the upper bound on electric field for quantum-well systems is pushed off significantly compared to the corresponding values for bulk materials.

It should be noted that redislocation may occur not only in an external electric field but may also be caused by a magnetic field [3], electromagnetic irradiation [4], or heat treatment [5].

2. The effect of electron wave function redislocation on the ionisation energy of an impurity atom can be understood within the effective mass method. The Schrödinger equation for the envelope $\Phi(\mathbf{r}, z)$ of the electron wave function is

$$\left[-\frac{\hbar^2}{2m}\left(\frac{\partial^2}{\partial \mathbf{r}^2}+\frac{\partial^2}{\partial z^2}\right)+U(z)-eFz+V(\mathbf{r},z)\right] \times \Phi(\mathbf{r},z)=F\Phi(\mathbf{r},z), \tag{1}$$

where e and m are the charge and the effective mass of the electron, $U(z)$ is the initial HS potential, $V(\mathbf{r}, z)$ is the potential produced by an impurity atom, and F is the electric field strength. The z axis is directed along the HS growth axis, $\mathbf{r} = (x, y)$.

The envelope of the wave function of an impurity-localised electron can be expressed as the expansion in terms of the eigenfunctions of Eqn (1) without the impurity potential. These are written in the form

$$\varphi_{n\mathbf{k}}(\mathbf{r}, z; F) = S^{-1/2}\psi_n(z; F)\,\exp(\mathrm{i}\mathbf{k}\mathbf{r}), \tag{2}$$

where S is the normalisation area (in the xy plane), $\psi_n(z; F)$ is the one-dimensional envelope function, n numbers the dimensional quantisation subbands, and $\mathbf{k}$ is the quasi-momentum of the free motion in the xy plane.

Let us consider the case of a strongly localised impurity potential which we represent by

$$V(\mathbf{r}, z) = -V_0 a^3 \delta(\mathbf{r})\,\delta(z - z_0). \tag{3}$$

Here z_0 is the coordinate of the impurity atom, and V_0 is the potential well depth, the lattice parameter a being incorporated into the definition of $V(\mathbf{r}, z)$ in order to preserve the necessary dimension. The potential (3) describes adequately the characteristic features of deep levels in semiconductors.

Lifshitz's equation for the potential (3) determines the energy of a localised electronic state and may be written in the form [6]

$$\frac{V_0 a^3}{(2\pi)^2}\sum_n\left[\left|\psi_n(z_0; F)\right|^2\int\frac{\mathrm{d}^2\mathbf{k}}{E_n(\mathbf{k})+E_{\mathrm{imp}}}\right]=1. \tag{4}$$

Here E_{imp} is the binding energy of an electron in the impurity centre. If only the lowest subband is taken into account, the binding energy may be expressed analytically in the following way:

$$E_{\mathrm{imp}}(F)=\frac{\pi^2\hbar^2}{2ma^2}\left[\exp\left(\frac{2}{wa\left|\psi_1(z_0; F)\right|^2}\right)-1\right]^{-1}, \tag{5}$$

where the dimensionless parameter $w = ma^2V_0/\pi\hbar^2$ may be considered as the effective power of the impurity potential. The factor $|\psi_1(z_0; F)|^2$ depends on both the impurity position in the HS and the electric field, and leads to a strong field dependence of the binding energy.

When two or more subbands are considered, a simple analytical solution of the type (5) for the binding energy is not possible, and Eqn (4) must be solved numerically. This requires a knowledge of the parameter w, which can be found if the volume magnitude of the binding energy $E_{\mathrm{imp}}^{(3D)}$ for the given impurity is known. Eqn (4) then yields $w = 1/(1 - \xi\,\mathrm{arccot}\,\xi)$, where $\xi = (2ma^2F_{\mathrm{imp}}^{(3D)}/\pi^2\hbar^2)^{1/2}$. The parameter w can also be gauged by an experimentally known value of the binding energy for an impurity state in a HS with a single quantum well of appropriate width.

3. The electric field also gives rise to the redislocation of the hole envelopes, leading to a number of new physical effects related to the binding energy of acceptor states [7]. For deep acceptors in specially chosen quantum-well systems, a severe change in the ionisation energy may occur even for fields which are small compared to those necessary for the effective redislocation of electron envelopes.

In fact, a one-dimensional potential modulating the top of the valence band in semiconducting quantum-well systems not only lifts the degeneracy of the valence band at the centre of the Brillouin zone, but leads to specific interference effects in the system of light- and heavy-hole subbands. The mixing of hole states in asymmetric quantum-well systems may change significantly the nature of the dispersion law in some of the subbands to the extent that even the sign of the effective mass may change. The nonparabolic effects in the dispersion law may become important even for relatively small values of the longitudinal (along the heterostructure layers) hole quasimomentum.

The mixing of the states pertaining, for example, to the first light-hole (LH1) and the second heavy-hole (HH2) subbands is most pronounced when the edges of these subbands come closest. In antisymmetric quantum-well systems, unlike single-square-well structures, the ordering of the LH1 and HH2 subbands depends heavily on the geometry of the heterostructure. Application of an external electric field may interchange the two, thus 'inverting' the hole spectrum. What is essential here is that close to the critical field point the mixing is strongest, and the subband which happened to be lowest in a given field, possesses an anomalous dispersion, i.e. a negative effective mass. In the vicinity of the so-called extremum loop thus formed, the density of states has a shape characteristic of one-dimensional systems. In AlGaAs/GaAs structures, the lower hole subband is the first heavy-hole (HH1) one, and therefore a dramatic change of the dispersion law in the HH2 subband affects significantly the binding energy of the acceptor states, which are split off from the heavy-hole band as a result of their symmetry.

4. Apart from the intrinsic interest in the modulation of the binding energy of impurity states, this effect is attractive in that it may serve as a basis for new high-performance quantum devices. A quantum-well system may be used as a channel for a field transistor with one of the wells acting as the electron pool. In contrast to known heterostructure field transistors, with the electron pool being the bulk of the semiconductor and the channel formation time determined by the relatively slow diffusion and drift processes, in the device proposed the channel formation time is determined by the electron tunnelling time from one quantum well to another. By appropriately choosing structure characteristics, the tunnelling time may be made extremely small.

The work of the device depends crucially on the change in the impurity ionisation energy caused by the redislocation of the electron wave function in the quantum-well system in an external electric field. The applied field transfers the wave function from a donor-doped quantum well into an undoped one. As a result, the coupling of the electrons to the impurities is broken, the impurity ionisation energy decreases, and the electrons move from the impurity atoms to the conduction band, thus forming a conducting channel in the field transistor. This changes considerably the concentration of free charge carriers and provides channel conductivity modulation necessary for the normal functioning of the transistor.

References

1. Bastard G *Wave Mechanics Applied to Semiconductor Heterostructures* (New York: Halsted, 1988)
2. Belyavskiĭ V I et al. *Pis'ma Zh. Eksp. Teor. Fiz.* **61** 1004 (1995) [*JETP Lett.* **61** 1039 (1995)]
3. Gorbatsevich A A, Kapaev V V, Kopaev Yu V *Pis'ma Zh. Eksp. Teor. Fiz.* **57** 565 (1993) [*JETP Lett.* **57** 580 (1993)]
4. Kopaev Yu V, Kornyakov N V *Mezhdunarodnyi Simpozium "Nanostruktury: Fizika i Tekhnologiya"* (International Symposium "Nanostructures: Physics and Technology") (St.-Petersburg, 1994)
5. Kapaev V V, Kopaev Yu V, Kornyakov N V *Pis'ma Zh. Eksp. Teor. Fiz.* **58** 901 (1993) [*JETP Lett.* **58** 843 (1993)]
6. Lifshitz E M *Zh. Eksp. Teor. Fiz.* **17** 1017 (1947)
7. Belyavskiĭ V I et al. *Pis'ma Zh. Eksp. Teor. Fiz.* **62** 197 (1995) [*JETP Lett.* **62** 208 (1995)]